Katarina Stiff Aamlid

Exploring the interaction abilities of Galectin-3 using the sensitive force probe optical tweezers

Outlining the structure-activity relationship by altering the modular architecture

Master's thesis in Chemical Engineering and Biotechnology
Supervisor: Marit Sletmoen

June 2020

NTNU
Norwegian University of
Science and Technology

Katarina Stiff Aamlid

Exploring the interaction abilities of Galectin-3 using the sensitive force probe optical tweezers

Outlining the structure-activity relationship by altering the modular architecture

NTNU
Norwegian University of
Science and Technology

Abstract

Glycans have the remarkable ability to display and store a high content of complex biological information, making them essential for several cellular activities. However, the complexity associated with the glycan structures has posed significant challenges in order to uncover their properties. Galectins are glycan-binding proteins (GBPs) characterized by specificity to β-galactosides. These molecules read and translate the information expressed by glycans and convert it into appropriate cellular responses. Currently, the glycan-GBP recognition regulating the specificity for the functional pairing is not completely outlined. Hence, an improved understanding of the glycan-GBP interactions is of interest in order to reveal the structure-activity relationship of these complex molecules.

This master thesis builds on and complements the work that was initiated in the master thesis of Sylvi Oliva Kjær in 2018. The scope of the present study was to investigate the interaction abilities of two different structural forms of Galectin-3 (wild-type and homodimer) using the glycoprotein asialofetuin (ASF) as a ligand. The galectins and glycoprotein were immobilized on polystyrene beads and the inter-molecular binding forces were quantified by using optical tweezers.

The results from this study confirm that ASF interacts with both Gal-3 WT and Gal-3 homodimer. By utilizing the Bell-Evans model it was possible to gain insight into the energy landscape of the two systems. Rupture forces were found to increase from 6.2 pN to 17.6 pN at loading rates between 39 pN/s and 406 pN/s for the Gal-3 WT - ASF system, and increase from 5.7 pN to 27.8 pN at loading rates between 38 pN/s and 309 pN/s for the Gal-3 homodimer - ASF system. Additionally, based on the parameters characterizing the energy landscape, it was identified that two energy barriers exist along the unbinding pathway for both systems. The comparison of the Gal-3 systems at low loading rates reveals that the Gal-3 homodimer exhibits higher rupture forces, longer lifetime and shorter separation distance compared to the Gal-3 WT. Since both structures of Gal-3 have identical binding sites, the differences can imply that Gal-3 WT is found as a monomer in solution, whereas the Gal-3 homodimer binds to the ligand through both the active binding sites.

Sammendrag

Glykaner har den unike evnen til å vise og lagre et høyt innhold av kompleks biologisk informasjon, noe som gjør dem essensielle for flere cellulære aktiviteter. Kompleksiteten forbundet med glykanstrukturer har likevel gitt store utfordringer med å avdekke deres egenskaper. Galektiner er glykanbindende proteiner (GBPs) som kjennetegnes ved sin spesifisitet til β-galaktosider. Disse molekylene leser og oversetter informasjonen uttrykt av glykaner til passende cellulære responser. Foreløpig har ikke glykan-GBP gjenkjennelsen som styrer spesifisiteten for den funksjonelle koblingen blitt fullstendig skissert. Dermed vil en forbedret forståelse av glykan-GBP interaksjoner være av interesse for å avsløre struktur-aktivitet forholdet mellom disse komplekse molekylene.

Denne oppgaven bygger videre og kompletterer arbeidet som ble initiert i masteroppgaven til Sylvi Oliva Kjær fra 2018. Målet med studien er å undersøke interaksjonsevnene til to forskjellige strukturelle former av Galektin-3 (villtype og homodimer) ved å bruke glykoproteinet asialofetuin (ASF) som ligand. Galektinene og glykoproteinet ble immobilisert på polystyrenkuler og de intermolekylære bindingskreftene ble kvantifisert ved brukt av optisk pinsett.

Resultatene fra denne studien bekrefter at interaksjoner oppstår mellom ASF og henholdsvis Gal-3 WT og Gal-3 homodimer. Ved å benytte seg av Bell-Evans modellen var det mulig å få innsikt i energilandskapet til begge systemene. Det ble funnet at bruddkreftene økte fra 6.2 pN til 17.6 pN for kraftlastrater mellom 38 pN/s og 406 pN/s for Gal-3 WT - ASF systemet, og økte fra 5.7 pN til 27.8 pN for kraftlasterater mellom 38 pN/s og 309 pN/s for Gal-3 homodimer – ASF systemet. I tillegg, basert på parameterne som karakteriserer energilandskapet, ble det identifisert at to energibarrier eksisterer for begge systemene. Sammenligningen av resultatene på de to Gal-3 systemene ved lave kraftlastrater, viste at Gal-3 homodimer oppnår høyere bruddkrefter, lengre levetid og kortere separasjonsavstand enn Gal-3 WT. Siden begge strukturene av Gal-3 har identiske bindingsseter, kan forskjellene antyde at Gal-3 WT blir funnet som monomer i løsning, mens Gal-3 homodimer binder seg til liganden gjennom begge de aktive bindingssetene.

Preface

This master thesis is submitted to the Department of Biotechnology and Food Science at the Norwegian University of Science and Technology (NTNU) and constitutes the completion of the Master of Science in Chemical Engineering and Biotechnology. This thesis is a continuation of the TBT4500 Biotechnology, Specialization project delivered fall 2019. Accordingly, the work has been carried out from August 2019 to June 2020. The experiments were performed in the laboratories at the Department Biotechnology and Food Science at NTNU. Due to the global pandemic, no experimental work was executed in the period middle of March 2020 to the end of April 2020. This limited the experimental work during this semester. All the figures without references are self-made in Inkscape and Sigmaplot.

First of all, I would like to give a major thanks to my supervisor Associate Professor Marit Sletmoen for the valuable and excellent guidance throughout the whole process. Additionally, I would thank both Ph.D. Candidate Ola Aarøen and Ph.D. Candidate Margrethe Gaardløs for assistance during challenges while working with the optical tweezers.

I would also thank Professor Hans-Joachim Gabius at the Ludwig-Maximilians University, Munich, for providing the protein samples.

Finally, I would like to thank my family and friends for all the support I have received from them.

Contents

List of Tables

List of Figures

List of Symbols

Table 1: List of Symbols

Symbol	Description	Unit
d	Displacement	[m]
F	Force	[N]
f^*	Most likely rupture force	[N]
f_0	Roll-off frequency	$[-]$
k	Spring constant/stiffness of the optical trap	[N/m]
k_B	Boltzmann constant	[J/K]
$k_{off,0}$	Dissociation rate	$[\text{s}^{-1}]$
k_{on}	Association rate	$[\text{s}^{-1}]$
$P(f)$	The unbinding force probability distribution	$[-]$
r_f	Loading rate	[N/s]
$S(t)$	Survival probability	$[-]$
T	Absolute temperature	[K]
t	Time	[s]
x	Length of compression or extension	[m]
x_β	Distance between bound and transition state	[m]
α	Trap stiffness	$[-]$
β	Sensitivty constant	$[-]$
τ	Bond lifetime	[s]

Abbreviations

AFM	=	Atomic force microscope
ASF	=	Asialofetuin
BSA	=	Bovine serum albumin
CRD	=	Carbohydrate recognition domain
DFS	=	Dynamic force spectrum
EDC	=	(N-(3-Dimethylaminopropyl)-N-ethylcarbodiimidehydrochloride
Gal-3	=	Galectin-3
GBP	=	Glycan binding protein
LacNAc	=	N-acetyllactosamine
MT	=	Magnetic tweezers
NA	=	Numerical aperture
OT	=	Optical tweezers
WT	=	Wild type

Chapter 1

Introduction

Development of new technologies to explore the structures and functions of glycans has provided a new frontier of molecular biology named glycobiology. Today, glycobiology is one of the more progressive fields in natural science containing a wide range of research areas, including biotechnology and biomedicine (Cummings and Vasta, 2017).

Glycans are the most abundant molecules found in living organisms, thus essential for life. They are assembled from simple sugar building blocks resulting in complexity and high information content. Every living cell is endowed with a dense and complex array of glycans that serve as a platform for the display of biochemical signals crucial for intercellular communication (Gabius, 2018). Specific glycan structures store a large amount of biological information, which can be translated into cellular function. However, until now, this mechanism is not fully examined and understood. Thereby, improved knowledge about the molecules that interpret the stored biological information in glycans, named glycan-binding proteins (GBPs), has to be achieved in order to eventually crack the sugar code. Their glycan specificity and their modular structure are supposed to be fundamental factors determining the profile of the functional outcome of glycan-lectin recognition (Kutzner et al., 2019). Galectin-3 (Gal-3) is a GBP with the specific binding of β-galactosides and participates in numerous biological processes including RNA splicing, apoptosis, cell migration, and cell differentiation. Additionally, Gal-3 has been found to contribute in several pathological activities such as cancer progression.

In this study, the galectin Gal-3 is investigated by comparing the binding abilities of two structural forms of Gal-3: wild type and homodimer, to bind the glycoprotein asialofetuin

(ASF). The proteins are immobilized on polystyrene beads and the inter-molecular binding forces are quantified by using optical tweezers (OT). The aim of this study is to enhance the understanding of the ligand binding to different structures of Gal-3 to outlining the underlying complex structure-activity relationship.

This master thesis is a continuation of a specialization project written fall 2019 for the department of biotechnology and food science at NTNU.

Chapter 2

Theory

The following chapter provides an introduction to the most relevant topics for understanding the principles in this research. Section 2.1 is an introduction to glycobiology with an emphasis on the lectins and glycan studied. The next section provides an introduction to the single-molecule force spectroscopy techniques with a focus on the three most commonly used techniques. While the last part explains how the information obtained from the single-molecule force spectroscopy techniques can be interpreted.

2.1 Glycobiology

In the broadest sense, glycobiology is defined as the study of the structure, biosynthesis, biology, and evolution of saccharides and the proteins that recognize them (Cummings and Vasta, 2017). All cells in nature carry an array of monosaccharides or oligosaccharides which are generally termed "glycans", and these are characterized by structural diversity (Cummings and Vasta, 2017). The variation of both composition and structure of the glycans is unsurpassed in nature because of the particular property to combine the following parameters with sequence independently: anomeric status, linkage positions, ring size, the addition of branches and site-specific introduction of substitutions (Gabius, 2017).

The glycan chains coated on the cell surface and secreted proteins are involved in crucial biological processes like interactions and communication between cells and the surrounding matrix. Through the glycosylation process, glycans covalently attach to other

biomolecules, such as lipids and proteins, and form glycoconjugates. The main classes of glycoconjugates are glycoproteins, proteoglycans, and glycolipids, all present on the cell surface (Cummings and Vasta, 2017), as illustrated in Figure 2.1. Molecules belonging to these classes together constitute the glycocalyx, a 10-1000 nm thick layer, which connects the inside of the cell with the outside environment (Huang and Godula, 2016).
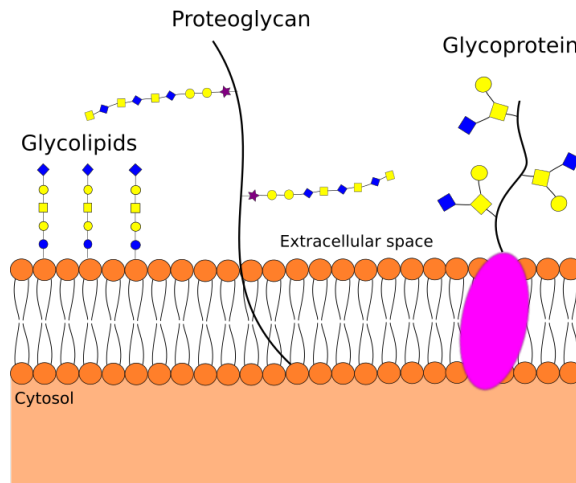
Figure 2.1: A simplified illustration of the main classes of glycoconjugates that decorate the cell surface and together making up the glycocalyx.

Glycans are specifically recognized by glycan-binding proteins (GBPs), also called lectins, which are characterized by a unique carbohydrate recognition domain (CRD). Lectins are found in every living organism ranging from viruses and bacteria to plants and animals. These proteins interpret and translate the biological information encoded within specific glycan structures into appropriate cellular responses, and in that way they bridge proteomics and glycomics (Dumic et al., 2006). Interactions between lectin and glycan structures are responsible for processes like protein folding and sorting, cell adhesion and trafficking, and pathogen recognition (Belardi and Bertozzi, 2015).

The interest of glycobiology has lagged behind other fields, such as genomics and proteomics, mainly due to the inherent complexity of glycans and lack of tools to study these molecules. However, over the past years, glycoscience has made a rapid progress due to the emergence of new technologies to study the structure and function of glycans, as well as lectin-glycan interactions (Cummings and Pierce (2014), Belardi and Bertozzi (2015)).

2.1.1 Galectins

The most widely expressed group of lectins are galectins, characterized by specific binding of β-galactosides through their $\sim$130 amino acid CRD (Johannes et al., 2018). According to the structure of the CRD, galectins are classified into three groups: chimeric (only galectin-3), prototypical (galectin-1, -2, -5, -7, -10, -11, -13, -14, -15, -16) and tandem repeat (galectin-4, -6, -8, -9, -12), illustrated in Figure 2.2. All containing a CRD with a highly conserved amino acid sequence and a β-sandwich structure. The prototypical galectins are characterized by a single CRD that can be associated as dimers. The tandem-repeat galectins are composed of two CRDs connected by a short peptide linker with up to 70 amino acids. While the chimeric group posses a collagen-like sequence that links the short 12 amino acid N-terminal domain to the CRD. The different galectins' affinity to various molecules differ. However, all of them have a high affinity for N-Acetyllactosamine(LacNAc)-based N- and O-linked glycans present in lipids, proteins, and other molecules (Seyrek et al., 2019).
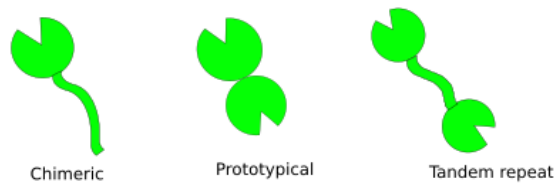
Figure 2.2: Illustration of the three different groups of galectins: chimeric, prototypical and tandem repeat.

Functionally, the galectins are involved in several processes, including inflammation, immune-response, RNA splicing, gene transcription, apoptosis, signaling, cell migration, and differentiation (Bartolazzi, 2018).

Galectin-3

Galectin-3 (Gal-3) is widely distributed through all the body and is found in tissues such as digestive tracts, lungs, blood, kidney, and heart (Díaz-Alvarez and Ortega, 2017). At the cellular level, the proteins are found within the nucleus, in the cytoplasm, on the cell surface and in the extracellular compartment. The proteins bind and interact with several ligands in the intra- and extracellular environment (Radosavljevic et al., 2012).

Gal-3 is structurally unique among all the galectins due to its C-terminal CRD linked to an N-terminal protein-binding domain, making it the only chimeric galectin (Díaz-Alvarez and Ortega, 2017). The C-terminal domain of Gal-3 contains about 130 amino acids creating a globular structure and are responsible for the lectin activity. The N-terminal domain consists of 110-130 amino acids, rich in proline and glycine (Dumic et al., 2006). Gal-3 can form a pentamer structure in the presence of multivalent ligands, containing five Gal-3 monomers linked together through the N-terminal domain (Ahmad et al., 2004). Normally, Gal-3 occurs as a monomer in solution, but it has also the potential to form homodimers by self-association in the absence of its ligands (Yang et al., 1998). The two structural forms of Galectin-3, monomer and pentamer, are illustrated in Figure 2.3.
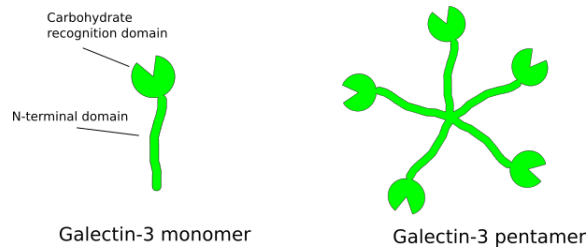
Figure 2.3: Illustration of the two structural forms of Galectin-3: monomer and pentamer.

The pentamer structures of Gal-3 can only form in the extracellular space, enabling Gal-3 to cross-linking glycoproteins and form lattices. Whereas, the monomer structures of Gal-3 can be found either in the cytoplasm or nucleus, participating in protein-protein and glycan-protein interactions (Farhad et al., 2018). Figure 2.4 illustrates some of the main extra- and intracellular functions of Gal-3.
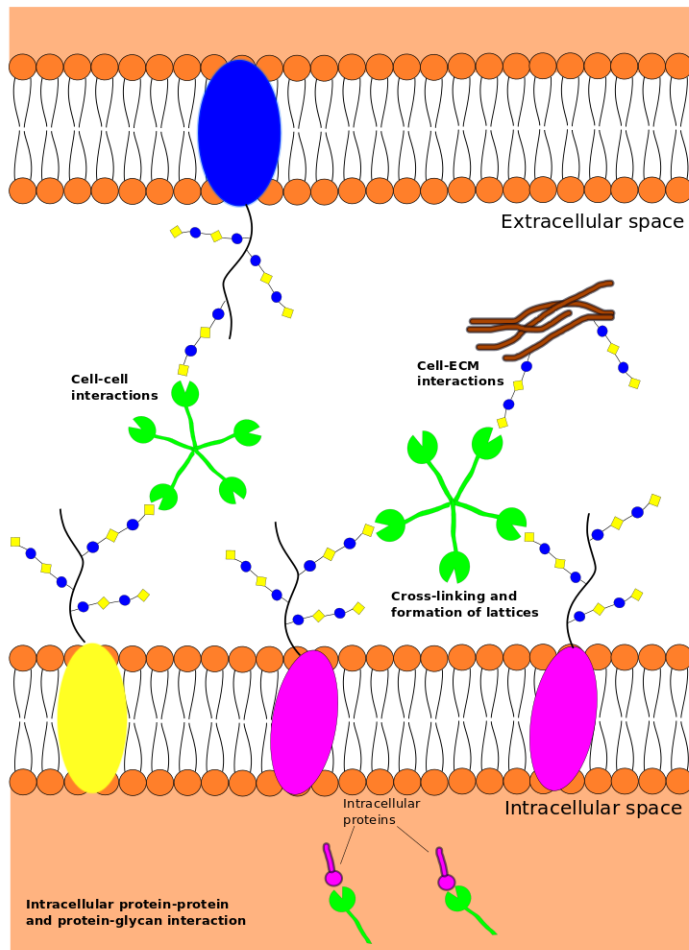
Figure 2.4: An illustration that displays some of the main extra- and intracellular functions of Gal-3, including cell-cell interactions, cell-ECM interactions, cross-linking, formation of lattices, protein-protein interactions and protein-glycan interactions.

Gal-3 is involved in several cellular processes, such as the regulation of cell growth, differentiation, apoptosis, regulation of RNA splicing and cell migration (Dumic et al., 2006). The various roles of Gal-3 on a cellular level lead to an array of consequences for several physiological and pathological processes, in particular, regulation of cancer progression,

inflammation, and immune response (Chan et al., 2018). Abnormal expression and location of Gal-3 are associated with the development, progression, and metastasis of cancer. Compared to normal tissues, the expression of Gal-3 has shown to increase in gastric, liver and thyroid cancers (de Oliveira et al. (2015), Sciacchitano et al. (2018)). The increased expression results in augmented suppression of the immune response. Thus, studies suggest that inhibition of Gal-3 together with established immunotherapy can both reduce immune suppression and decrease tumor growth (Linch et al. (2015), Farhad et al. (2018))

Galectin-3 homodimer

To enable the identification of the principles of the relationship between structure and activity underlying the specificity of recognition and the followed binding process of the galectins, the architecture of their CRD has been emphasized. By utilizing Gal-3 as a model, protein engineering has used its CRD to build variant proteins with different modular assembly (Caballero et al., 2020).

As mentioned in the previous section, the natural Gal-3 creates its own group of galectin architecture due to its unique structure, i.e. the CRD attached to the N-terminal tail. However, this natural Gal-3 can be converted into a homodimer, hence switching its class. This is accomplished through engineering on the level of cDNA by directly joining two Gal-3 CRDs, providing Gal-3-Gal-3, or by putting a linker of a tandem repeat type galectin-8 (33-aa S or 74-aa L), yielding the Gal-3-8S or L-Gal-3 variants, respectively (Ludwig et al., 2019), as illustrated in Figure 2.5.

Figure 2.5: Illustration of the different engineered variants of Gal-3, where the chimeric Gal-3 is switched into a homodimer.

A recent study conducted by Caballero et al. (2020) converted the chimera-type Gal-3 into a pair of homodimers (Gal-3 - Gal-3 and Gal-3 - 8S - Gal-3) to determine the properties of Gal-3's CRD presented in the different structural forms. The results of the binding of LacNAc to the galectins revealed that Gal-3 homodimers have a similar affinity as measured for the Gal-3 WT monomeric in solution.

In order to identify the design-dependent functionality of Gal-3's CRD, pair building of wild type and variant proteins facilitate the comparative analysis (Ludwig et al., 2019).

2.1.2 Asialofetuin

In the current research, the naturally occurring human glycoprotein asialofetuin (ASF) was used as a binding ligand for both structures of Gal-3. ASF is a multivalent glycoprotein that expresses three N-linked triantennary chains with nine LacNAc epitopes, each found to interact with Gal-3. Consequently, ASF has the ability to binding nine galectin molecules (Dam et al., 2005).

Glycan chains of numerous naturally occurring glycoproteins have usually more than one copy of the carbohydrate epitope, and are thus said to be multivalent. One effect of the multivalency is to augment the affinity of a glycoprotein for specific binding receptors, such as lectins. Glycoproteins can possess two types of multivalency: the glycoprotein can consist of asparagine (N^1)- or serine/threonine (O)-linked carbohydrate chains that are multivalent, or several glycan chains at various sites can provide the glycoprotein multivalency. ASF has both types of multivalency, hence increasing the affinity for its specific binding partners (Dam et al., 2005).

ASF is a ligand molecule selectively recognized by asialoglycoprotein receptor, which is in large numbers present on hepatocytes, and ASF is entering the cell through the receptor (Arangoa et al., 2003). Therefore, ASF has been investigated as a ligand to deliver drugs to hepatocytes and used in gene therapy by specific targeting the liver (Motoyama et al. (2011), Farinha et al. (2014)).

2.2 Single-molecule force spectroscopy techniques

The field of glycobiology research has increased significantly due to the attempt to elucidate the roles of glycan structures in biology. The emphasis of this field has been to understand the evolution, biosynthesis and interactions of glycans, both individually and as a part of larger biomolecules (Lakshminarayanan et al., 2018). Glycan interactions involve molecular forces, thus single-molecule force spectroscopy techniques are becoming suitable tools in glycoscience to quantify the forces arising during a single glycan interaction. The quantification of these forces provides a measure of the properties such as bond energies, lifetimes and the energy landscape of the specific interaction.

Single-molecule force spectroscopy enables to study the forces and enzymatic activity of molecules. Biological processes ranging from cell motility to segregation of DNA are based on the molecular-scale forces, providing forces a crucial role (Neuman and

Nagy, 2008). The techniques have the potential to examine the force-dependent properties of molecular complexes, including receptor-ligand bonds, viscoelastic properties of molecules such as protein unfolding, and force generation by molecular motors (Johnson and Thomas, 2018).

The most commonly used methods are atomic force microscopy (AFM), optical tweezers (OT) and magnetic tweezers (MT). These techniques enable the measuring of forces formed by a few hydrogen bonds and up to forces required to separate two adhering cells (Dufrêne et al., 2011). Thus, they have a broad spectrum of applications in the study of molecular processes where forces play a fundamental role.

In the present research, OT was utilized to quantify the interactions between ASF and the two Gal-3 structures, respectively. This technique will be outlined in detail in the following section. Further, the two other techniques, MT and AFM, will be described.

2.2.1 Optical tweezers

OT, also called an optical trap, are among the most versatile single-molecule manipulation technique. It has the ability to apply forces of 100 pN on particles ranging in size from nanometers to micrometers. Simultaneously, it measures the three-dimensional displacement of the trapped particle with sub-nanometer accuracy and sub-millisecond time resolution. Additionally, OT possesses the advantage to investigate forces down to 10 pN (Neuman and Nagy, 2008).

OT was developed by Arthur Ashkin in 1970, after observing that micron-sized particles could be trapped by the force of radiation pressure from a laser beam (Ashkin, 1970). An optical trap is formed by a highly focused laser beam with an objective lens of high numerical aperture. Two forces are acting on a dielectric particle located in the focus of the laser beam: the scattering force and the gradient force. The scattering force works in the direction of light propagation, while the gradient force works in the direction of the spatial light gradient. To obtain stable trapping in all three dimensions the gradient force must exceed the scattering force, which is accomplished by a tightly focusing laser (Neuman and Block, 2004). The general setup of OT is present in Figure 2.6.
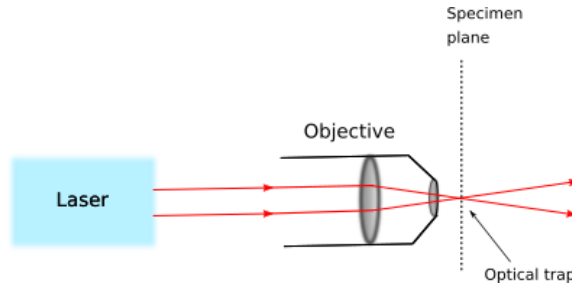
Figure 2.6: A simplified illustration of the general setup of OT. The laser generates two separate laser traps, enable to trap one particle each.

If aiming to use the OT setup to quantify interaction forces, the setup must be calibrated. The main goal of calibrating is to determine the trap stiffness and measure the absolute displacements of the trapped particles (Polimeno et al., 2018). Position and force calibration of OT is gained by the probe being treated as a linear spring and the force is calculated from Hooke's law (Eq. 2.1),

$$F = -kx \tag{2.1}$$

where F is the force, x is the length of compression or extension and k is the proportionality constant, known as the spring constant or trap stiffness. The photodiode generates the distance, x, as illustrated in Figure 2.7. Typically, the calibration of the position detector is accomplished by moving the trapped bead through a known distance while recording the position signal. The simplest and most commonly used calibration method of trap stiffness is based on thermal fluctuations of the trapped bead, which is equal to the Brownian motion of an over-damped spring. The power spectrum of the fluctuations is Lorentzian containing a roll-off frequency, f_0, which is defined in the following equation:

$$f_0 = \frac{1}{\alpha(2\pi\beta)} \tag{2.2}$$

where α is stiffness of the trap and β is the hydrodynamic drag on the bead. By fitting the power spectrum the roll-off frequency can be achieved (Neuman and Nagy, 2008).
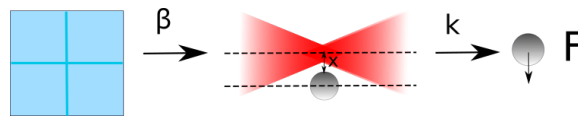
Figure 2.7: A schematic illustration that shows how the conversion factors are related to each other in order to determine the forces that act on the particle trapped by the laser in the OT. The photodiode detects the changes in the intensity photons which are converted into a displacement coordinate, x, of the particle by the sensitivity constant, β, determined from the calibration. The displacement, x, is converted into force by multiplying it with the stiffness of the optical trap, k.

Despite the versatility and precision of OT, some limitations are associated with using light to generate force. The performance can degrade due to the optical perturbations that affect the intensity, since the trap stiffness relies on the gradient of the optical field. Hence, the high-resolution optical trapping is limited to optically homogeneous preparations and highly purified samples. Additionally, OT lack sensitivity and exclusivity. This means that any dielectric particle located near the focus of the trapping laser will be trapped, and therefore can several particles be trapped simultaneously. To avoid this the concentration of freely diffusing particles in the sample must be kept very low. Another challenge related to OT is the local heating generated by the high intensity at the focus of the trapping laser. This can affect the enzymatic activity and alter the local viscosity of the medium. A less well understood limitation of OT is optical damage. By now, trapping with laser wavelength in the near-infrared wavelengths have shown to be the most successful in order to minimize the photodamage. However, an oxygen-mediated photodamage process remains even in this wavelength range (Neuman and Nagy (2008), Blázquez-Castro (2019)). Further, the photodamage can be reduced by removing the molecular oxygen from the trapping medium, or exchanging the oxygen with an inert gas (Neuman et al., 1999).

OT have numerous applications at the interface of physics and biology. The technique has the ability to measure forces of smaller magnitudes than the forces that can be determined using AFM, because of the lower spring stiffness (Neuman and Nagy, 2008). When studying interactions between biological molecules a dual-trap mode is convenient to use, meaning that the laser beam is split into two separate beams. Hence, the two optical traps enable the probing of multiple particles simultaneously.

2.2.2 Atomic force microscopy

The AFM was first introduced in 1986 (Binnig et al., 1986) and the tool was considered as a breakthrough in nanotechnology (Gerber and Lang, 2006). The technique permits biological samples, ranging from single molecules to living cells, to be visualized and manipulated (Dufrêne et al., 2017). Thus, AFM is an ideal tool for biological applications, such as ligand binding, antibody-antigen interactions, and protein unfolding. (Pfreundschuh et al. (2015), Ouerghi et al. (2002), Mitsui et al. (1996)). AFM is mainly an imaging tool. However, it also allows measurement of inter- and intramolecular interaction forces with piconewton resolution (Neuman and Nagy, 2008).

The AFM consists of a cantilever with a sharp tip located at the end which scans the surface of a sample to create a topographic image of the sample. An optical detector of high precision (a quadrant photodiode) detects the cantilever deflections caused by interactions with the surface and senses a laser beam reflected from the cantilever's backside (Li et al., 2017). The general setup of the AFM is illustrated in Figure 2.8. The binding of one type of molecules to the surface of the cantilever tip and a second type of molecules to the surface enables the quantification of the interaction force between the two types of molecules. Based on the force curves it is possible to determine the interaction forces. These curves reveal the deflection of the cantilever as a function of the separation distance between the tip and the surface. (Safenkova et al., 2012). Generally, the force is calculated from the detected bending of a cantilever of known spring constant. The cantilever stiffness relies on the properties and shape of the cantilever's material, with typical values between 10^1 - 10^5 pN/nm. The spring constant of each cantilever must be correctly calibrated before use to achieve precise force data (Neuman and Nagy, 2008).
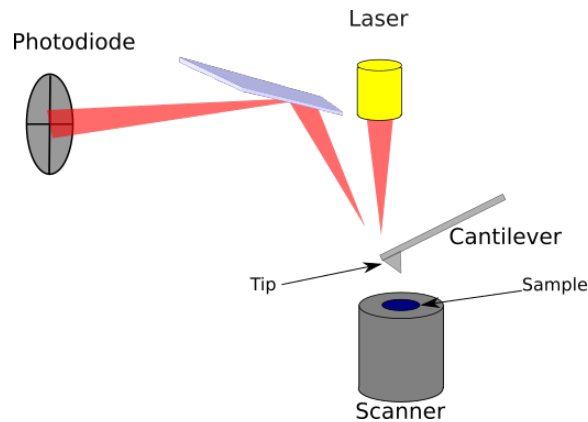
Figure 2.8: A schematic illustration of the setup of the AFM instrument. The tip attached to the cantilever scans across the sample surface. A laser beam pointing at the tip of the cantilever reflects and is detected by a photodiode detector.

The advantages of AFM are simple and rapid sample preparation, including the ability to carry out measurements of biological samples under near-physiological conditions. However, there are some drawbacks, such as the large size and relatively high stiffness of the cantilevers. These drawbacks impose a lower bound on the useful force range and reduced bandwidth, especially in aqueous solutions. Thereby, many forces linked with several biological processes could be challenging to study with AFM (Neuman and Nagy, 2008).

2.2.3 Magnetic tweezers

Since the invention of MT, the single-molecule technique has developed rapidly with a broad range of applications. Compared to OT and AFM, the implementation of MT is more straightforward by requiring only a limited number of optical components, an apparatus which is relatively drift-insensitive and spatial information through camera-based detection (Neuman and Nagy (2008), Dulin et al. (2015)). The MT enable the manipulation of paramagnetic beads by using a gradient of a magnetic field (Strick et al., 1996).

The setup of MT contains a pair of permanent magnets located above the sample holder of an inverted microscope equipped with a charge-coupled device camera which is connected to a frame grabber. The principal of MT are common to the OT: a magnetic particle placed in an external magnetic field is exposed to a force proportional to the gradient of the square of the magnetic field. The technique is able to apply both forces and torques to tethered molecules. It can easily apply and measure forces in the range from 100 pN down to 10

fN, and rotates particles in the size of 0.5 μm to 5 μm. A single magnet is utilized when supplying an attractive pulling force on a magnetic particle, however, a minimum of two magnets are required to create torque and apply force (Yu et al. (2014), Neuman and Nagy (2008)). Figure 2.9 illustrates the general setup of the MT.
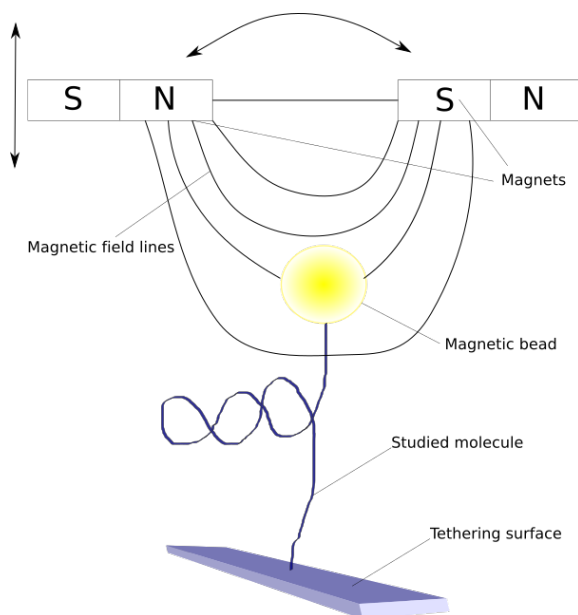
Figure 2.9: A schematic illustration of magnetic tweezers. A molecule is tethered between the magnetic bead and tethering surface. The magnets above the trapping chamber form a magnetic field along the axial direction, which produces a force on the bead in the direction toward the magnets.

To obtain quantitative data, the MT require an accurate force calibration (Ostrofet et al., 2018). There are two approaches of force calibration that can be performed. The first method is based on the determination of the force from the gradient of the product between the magnetization of the bead and the magnetic field. The second approach relies on the sampling of the Brownian motion of a tethered magnetic bead. The force can be determined from the variance of the transverse fluctuations, as well as the calculation of the tether length (Yu et al., 2014).

In contrast with OT, magnetic tweezers do not experience problems such as photo damage and sample heating. However, the technique is not as versatile as OT and AFM. The robust permanent magnet configuration lacks the ability to manipulate. Even though the ability to rotate magnetic beads has shown to be an useful feature, the massive applied torque

prevents the direct measure of rotation and torque generation (Neuman and Nagy, 2008). Additionally, the camera-based detection is limited in the measurements of temporal and spatial resolution (De Vlaminck and Dekker, 2012)).

2.3 Dynamic force spectroscopy

The inter-molecular bonds between molecules are primarily arising from non-covalent interactions, such as hydrogen bonds, Van der Waals interactions, π-π bonds, electrostatic interactions and hydrophobic interactions. These bonds are characterized with a limited lifetime, meaning that the bond will rupture when an external force is pulling on them for a sufficient time and strength (Evans, 1999). The rupture forces of interactions can be quantified by using different sensitive force probes such as OT, MT and AFM. Further, the interaction properties can be analyzed through the method of dynamic force spectroscopy (DFS). This method yields information about the energy landscape of the interaction, including estimates of parameters like the lifetime of the bond and free energies of transitions between a bound state and an unbound state (Evans and Ritchie, 1997). In the DFS method, the inter-molecular bonds are exposed to an external force that increases with time, and this is defined as the loading rate, r_f:

$$r_f = \frac{\Delta f}{\Delta t} \tag{2.3}$$

The rupture force of the inter-molecular bond is achieved as a function of the loading rate, providing a scatterplot that shows the relationship between the rupture force (pN) on the y-axis and the logarithm of the loading rate (pN/s) on the x-axis. This plot forms a dynamic spectrum of bond strengths and yields information about the specific energy landscape along the unbinding pathway. Due to the stochastic nature of non-covalent interactions, a great number of observations must be achieved in order to provide robust estimates of the parameters that characterize the energy landscape (Håti et al. (2015), Evans (1999)).

Molecular interactions can create several different conformation states and each state is associated by a specific energy amount. The certain amount of energy needed in order to leave a bound state is defined as the activation energy. During dissociation of molecular bonds, the bond has to exceed one or several activation energy barriers, characterizing the energy landscape of the interaction. A stable state is the state a bond will preferably stay in, and it is the state with the least possible Gibbs free energy involved. When the bond is manipulated due to the exposure of an external force, it is forced to alters to states

with a higher degree of energy, called transition states. This is caused by disrupting and formation of new interactions until the two molecules are fully unbound (Evans, 1999). Figure 2.10 illustrates the free energy landscape for a dissociation process of a molecular complex, showing that when the bond is exposed to an external force, it adds mechanical potential that tilts the energy landscape and lowers the barriers.
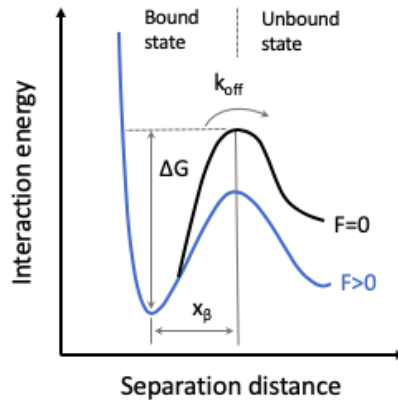
Figure 2.10: A graphical illustration of a free energy landscape with a single barrier unbinding process. An external applied force, F, alters the unbinding barrier and the dissociation rate, k_{off}. The activation free energy is ΔG and the distance between the bound state and transition state is x_β.

Normally, molecular interactions consist of several energy barriers which the molecule has to exceed to obtain binding or unbinding. The energy barriers can be observed in the most probably rupture forces vs. $\ln r_f$ plot, containing multiple linear regimes with ascending slopes. Accordingly, the graph has to be fitted to all the linear regions, where each linear region will represent an energy barrier (Evans, 1999). Figure 2.11 illustrates a simplification of a DFS-plot where the change in the linear slope is a result of the existence of two energy barriers of the interaction between two molecules.
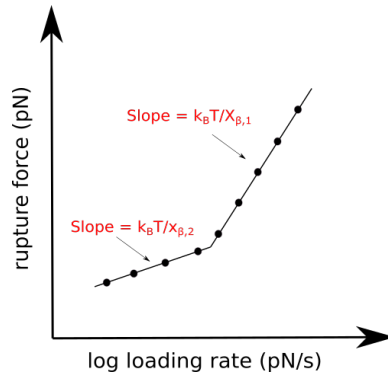
Figure 2.11: A simplified illustration of a DFS-plot showing interaction forces between two molecules, where rupture forces are on the y-axis and $\ln(r_f)$ on the x-axis. The abrupt change in slope demonstrates that two energy barriers exist. The x_β-values can then be extracted from the two slopes.

Interactions between two molecules, A and B, with equal affinity for each other creating a complex, AB, are described by the following equation:

$$\frac{d[AB]}{dt} = k_{\text{on}}[A][B] - k_{\text{off}}[AB] \tag{2.4}$$

where [A], [B] and [AB] show the concentration of the two molecules and the complex, respectively. While k_{on} and k_{off} is the association rate and the dissociation rate, respectively (Bizzarri and Cannistraro, 2010). By exposing the molecular bond with an external force, the energy landscape alters, resulting in lower activation energy. According to Bell's assumptions, a decrease of the activation free energy for a reaction of zero force is proportional by a factor of applied force, f. Given this assumption and Equation 2.4, the dissociation rate at applied force, $k_{\text{off},0}(f)$, increases exponentially according to the following equation:

$$k_{\text{off},0}(f) = k_{\text{off}}(0)exp(\frac{f x_\beta}{k_B T}) \tag{2.5}$$

where $k_{\text{off}}(0)$ is the dissociation rate at zero force, x_β is the reaction coordinate that corresponds to the distance between the bound and the transition state, k_B is Boltzmann constant and T is the absolute temperature. Additionally, x_β is assumed to not be affected by the force. Due to the decrease of k_{off}, the bond lifetime, τ, is shortened by the given equation:

$$\tau = \frac{1}{k_{\text{off}}} \tag{2.6}$$

Richie and Evans developed the Bell-Evans model as a result of Bell's assumptions, that explains the experimentally measured distribution, P(f), of rupture forces with time-dependent force, f(t). Hence, the model describes the dependence of the unbinding force on the loading rates (Evans and Ritchie, 1997). The model is based on several assumptions: 1) the loading rate, r_f, is constant during the measurements, 2) only a single pair of molecules that interact is investigated during the process, 3) the rupture time is longer than the diffusional relaxation time, 4) the rebinding process is neglected and 5) the pulling force and the reaction coordinate, x, works in the same direction (Bizzarri and Cannistraro, 2010). Consequently, the survival probability, S(t), of the process at time t, is given by the following equation:

$$S(t) = exp\left[-\int_0^t k_{\text{off}}(t')dt' \right] \tag{2.7}$$

where $k_{\text{off}}(t)$ is the time-dependent dissociation rate. This equation provides the ability to calculate the probability that the unbinding process of the molecules not yet has occurred at a time, t. S(t) is associated with the unbinding force probability distribution, P(f), by the following equation:

$$P(F)dF = -S(\tau)d\tau \tag{2.8}$$

where τ is the lifetime of the bond. Given Bell's assumptions and by performing the integral, P(f) is described by the following equation:

$$P(f) = \frac{k_{\text{off}}}{r_f} exp\left[\frac{fx_\beta}{k_BT} + \frac{k_{\text{off}}k_BT}{x_\beta r_f} \left(1 - exp\left(\frac{fx_\beta}{k_BT} \right) \right) \right] \tag{2.9}$$

By calculating the maximum of Equation 2.9, the most probable unbinding force, f*, at a specific value of the loading rate, r_f, is obtained:

$$f^* = \frac{k_BT}{x_\beta} ln(\frac{r_f x_\beta}{k_{\text{off}} k_BT}) \tag{2.10}$$

Equation 2.10 illustrates the linear relationship between the most probable rupture force and the logarithm of the loading rate. Thus, by measuring these two variables experimentally, the dissociation rate at zero force, $k_{\text{off}}(0)$, and the distance from the free energy

minimum to the energy barrier, x_β, can be found from the slope and intercept of the fitted linear plot, respectively. If aiming to understand the thermodynamic and kinetics of the interaction between a molecular pair, these parameters are crucial (Evans and Ritchie (1997) Evans (1999)).

Chapter 3

Materials and Methods

3.1 Materials

The following list shows the materials and chemicals that were used in this experiment:

- Asialofetuin (ASF)

- Boric acid (H_3BO_3), pH 5.8, Sigma-Aldrich, CAS number: 10043-35-3

- Borosilicate Glass (22x50 mm), VWR, Cat number: 631-0137

- Bovine Serum Albumin (BSA), Sigma-Aldrich, CAS number: 9048-46-8

- COOH-functionalized polystyrene beads, diameter 3.07 μm, Spherotech

- EDC (N-(3-Dimethylaminopropyl)-N-ethylcarbodiimide), Sigma-Aldrich, CAS-number: 1892-57-5

- Galectin-3 homodimer

- Galectin-3 WT

- HEPES buffer (4-(2-Hydroxyethyl)piperazine-1-ethanesulfonic acid), pH 7.2, Sigma-Aldrich, CAS number: 7365-45-9

- NH_2-functionalized polystyrene beads, diameter 2.18 μm, Spherotech

ASF, Gal-3 WT and Gal-3 homodimer were kindly provided by Professor Hans-Joachim Gabius, Ludwig-Maximilians University, Munich.

3.2 Protein immobilization on the polystyrene beads

In order to trap and analyze the proteins in the OT, the galectins and glycoproteins were immobilized on the surface of the polystyrene beads. Two different stock solutions were prepared, one with the galectin and the other with the glycoprotein, for further sample preparation. The proteins provided in solid-state were diluted with HEPES buffer (100 mM HEPES, pH 7.2, 150 mM NaCl) to a final concentration of 2 mg/ml. Then the stock solutions of galectin and glycoprotein were added into separated eppendorf tubes and immobilized on the polystyrene beads by mixing 2.5 μL of the stock solution with 50 μL boric acid (50mM, pH 5.8), 3 μL of functionalized polystyrene beads and 0.4 mg EDC. To distinguish between the beads two different sizes were used. For the galectin stock solution, COOH-functionalized polystyrene beads with a diameter of 3.07 μm were utilized. While for the ASF stock solution, NH$_2$-functionalized polystyrene beads with a diameter of 2.18 μm were used. EDC is used as an activating reagent and facilitates the reaction between the carboxylic acid and amine groups. The mixtures were left for 45 minutes to allow the EDC to function, followed by washing the beads 5 times through centrifugation, for 6 minutes and 7500 rpm. Between every centrifugation, the supernatant was discarded and the pellet was resuspended in 50 μL HEPES buffer. After the last centrifugation, the pellet was resuspended in 150 μL HEPES buffer.

3.3 Preparation of the liquid cell

A liquid cell with the final sample was made in order to be investigated in the OT instrument. The liquid cell contains a circular BSA-coated glass attached to a rectangular glass plate by two strips of double-sided tape, as illustrated in Figure 3.1. A space of approximately 2 mm was formed where the finale sample solution was injected into by capillary forces. The circular glasses were covered with BSA to prevent the functionalized beads from adhering to the glass slip. The BSA-coated glasses were prepared by cover them with filtered BSA solution (1 mg/mL, 0.1 μm filter) and then incubated for 20 minutes. The excess of the BSA solution was removed by a pipette, followed by drying them completely with N$_2$ gas. The final sample solution was prepared by mixing 2.5 μL of each bead solution with 100 μL HEPES buffer in an eppendorf tube. 15 μL of this final sample solution was used to fill up the liquid cell. Finally, nail polish was added on both ends to prevent evaporation of liquid.
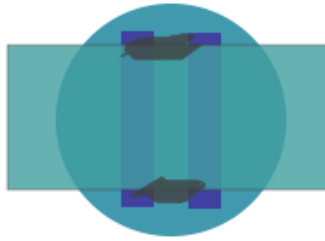
Figure 3.1: Illustration of the liquid cell containing a BSA-coated circular glass attached to a rectangular glass with two strips of double-sided tape (dark blue). Each ends are sealed with nail polish (black) to prevent evaporation.

3.4 The set up of optical tweezers

In this experiment, the Nanotracker OT instrument, illustrated in Figure 3.2, delivered by JPK instruments was used. The instrument is integrated with a Zeiss Axio Observer Inverted microscope and equipped with a TEM_{00} laser containing a maximal power of 3W. The laser has a Gaussian beam profile and the ability of dual-beam mode with scalable split-ratio. The two traps have the opportunity to be controlled separately from each other. The displacement of the trapped beads is detected by a quadrant photodiode located on the back focal plane of the condenser. Also, the software "Nanotracker 2.0" is delivered by JPK instruments and is utilized to control and record force data. In order to minimize and prevent noise in the form of vibrations from the floor, the OT instrument is placed on a vibration isolated table.
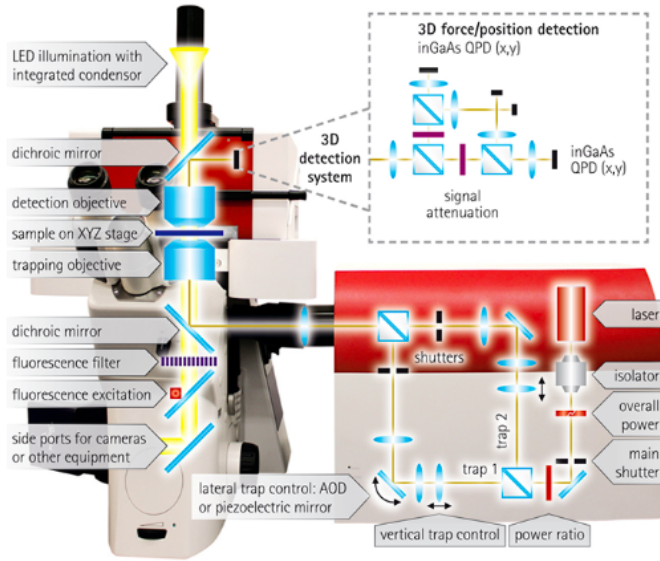
Figure 3.2: Illustration of the NanoTracker Optical Tweezers delivered by JPK instrument that is used in this experiment (Instruments, JPK, n.d.)

3.5 Calibration of optical tweezers

The liquid cell injected with the final sample solution was placed on the sample stage inside the OT. To obtain an optimum illumination of the sample was a Köhler illumination performed. The position of the objective was set to an optimal focus of the beads. Further, two beads of different sizes were trapped in each laser (2.18 μm and 3.07 μm) and the different diameter sizes were inserted into the calibration manager. The beads were calibrated in all directions (x, y and z) to determine the trap stiffness and sensitivity, allowing the QPD signal to be converted from volt to force. This was accomplished by the calibration function in the NanoTracker software. The program does eight recordings of the Brownian motions of the beads and determines a spring constant, as well as suggesting a Lorentzian fitting curve, S(f). Based on this fitting curve, the sensitivity and the stiffness are derived. If there is a low correlation between the fitting curve and the recorded data, the bead was discarded because this may indicate a defect on the bead. Thus, another bead should be used for the final recordings.

3.6 Data collection

Before the force measurements were started, several parameters had to be determined. This includes the displacement and speed of the moving bead, as well as the z-position of the beads and the pause time when the beads are in contact. During the experiments, the displacement was set to approximately 2.5 μm with a varying speed between 1.0-2.0 μm/s and pause time between 0.3-0.8 s. During the collection of the force data, one of the beads was kept stationary while the other approached and retracted from it, in an oscillating movement. This provided force curves that show the relationship between the force (pN) and the bead displacement from the start position (nm) for each oscillation.

3.7 Data processing

The force curves achieved from the OT analysis were further analyzed with four programs: iNanoTrackerOT3DPreProcess3a.pro, iNanoTrackerOT3DPostProcess2.pro, iNanoTrackerGallery.pro and ForceSpecAnalysev8.pro. All written by Bjørn Torger Stokke, Professor at the Department of Physics at NTNU and all run by the IDL Data Visualization Software.

First, the generated force files from Nanotracker were processed by the pre-process program, which combines the retraction and approach curves from both beads and generates a single position-coordinate, using Eq. 3.1 and 3.2. Additionally, the pre-process program evens out the baseline, providing a force curve with a straight and horizontal baseline, which facilitates further analysis.

$$\Delta = F(retract) - F(approach) \tag{3.1}$$

$$\sum F = \Delta F_x + \Delta F_y + \Delta F_z \tag{3.2}$$

The new combined curves generated from the pre-process program were further analyzed in the post-process program, where the curves with interaction were separated from those without. Also, the slope of the curve with interaction could be manually fitted. Based on this curve is the rupture force, f*, and the loading rate, r_f, determined. The rupture force, f*, is found from the height of the force peak relative to the baseline. Curves that contain multiple peaks indicate that multiple bindings have been ruptured. The loading rate, r_f, is defined as the external force applied per unit time (*df/dt*), and can be calculated by using Eq. 3.3:

$$r_f = \frac{\Delta y}{\Delta x} = \frac{\Delta f}{\Delta d} \qquad (3.3)$$

where Δd is the displacement of the beads in nm.

In order to make galleries of the generated curves, the program iNanoTrackerGallery.pro was used. While the rest of the graphs were made in SigmaPlot. The program, Force-SpecAnalysev8.pro, was used to generate DFS-plot, splitting the data into histograms and calculate the energy landscape parameters.

To obtain the parameters of the energy landscape, two different approaches were used. In Method 1 (no constraints), f^*, $k_{off,0}$ and x_β were determined based on a fit of P(f) (Eq. 2.9) to the histogram distributions. For the other approach, Method 2, the slope of the linear regimes in the DFS is determined, and the slope is defined as $\frac{k_B T}{x_\beta}$. A constrained fit was achieved by feeding the value of x_β obtained using this approach into P(f). The value of x_β, $k_{off,0}$ and f^* achieved using this approach could be then compared to the values obtained from Method 1.

Chapter 4

Results

The experimental data obtained as part of this study builds on and complements previous data obtained by Sylvi Oliva Kjær and published as part of her master thesis (Kjær, 2018).

The force curves generated by the OT instrument enable the visualization of the interactions between ASF and the galectins by using polystyrene beads functionalized with the galectins and glycoprotein. The force curves demonstrate how the forces acting on the polystyrene beads alter with increasing inter-bead distance (nm) that is caused by the polystyrene beads' separation in the optical traps. When the two beads are in contact, inter-molecular bonds can form between the galectin immobilized on one bead and its ligand immobilized on another bead. Force jumps in the recorded curves are observed if interactions occur.

Based on the obtained rupture events a DSF-plot for each system is generated. These plots show the relationship between rupture force and the logarithm of the loading rate. Subgroups of datapoints were made by defining intervals along the axis of increasing loading rate. Further, these subgroups were analyzed by generating histograms that show the distribution of the rupture forces within an interval of loading rates. The probability density function, P(f) (Equation 2.9), for each interval was determined and fitted to the histogram distribution. Through the fitting procedure, the most likely rupture force, f* (Equation 2.10), and the average loading rate, r_f, were determined for each interval.

In the following chapter are the results obtained from the investigation of interactions between two structural forms of Gal-3 (wild type and homodimer) and their ligand ASF by

using OT presented. Section 4.1 and 4.2 present the experimental data from the interactions of Gal-3 WT and ASF and Gal-3 homodimer and ASF, respectively. Both sections include galleries of force curves, DFS-plots, histograms for each subgroup of loading rate and the parameters that characterize the interactions. Section 4.3 presents a comparison of the experimental data obtained from the two systems.

4.1 Experimental data for Gal-3 WT - ASF interactions

In this part of the study, the substrate binding abilities of Gal-3 WT were investigated by using ASF as a substrate. The analysis of the data obtained from the OT retraction experiments enables the generation of the force curve galleries and the DFS-plot, as well as the parameters describing the interaction. This section presents the experimental data obtained from the interactions between Gal-3 WT and ASF. The new data obtained from the current study builds on the previous data obtained by Sylvi Oliva Kjær (Kjær, 2018).

Figure 4.1 shows a comparison of the data obtained from this thesis with previously obtained data by Sylvi Oliva Kjær for the rupture force and loading rate of the Gal-3 WT - ASF system. The previous results are indicated in red colour, while the results obtained in this study are indicated in green colour. The data set from the present study depicts a higher loading rate compared to the data set from the previous study.
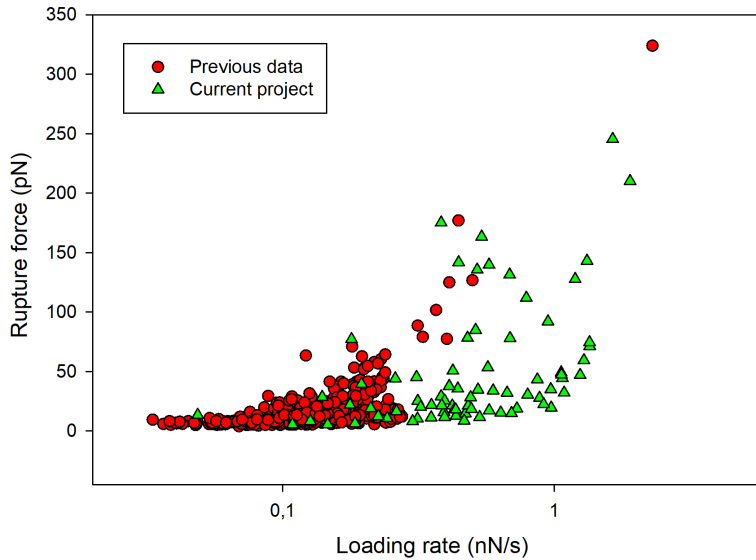
Figure 4.1: The rupture force plotted against the loading rate for the experimental data of Gal-3 WT - ASF system obtained from Kjær's thesis (red colour) compared to the results from the current study (green colour).

4.1.1 Galleries

Figure 4.2 and Figure 4.3 present force curves with events of higher rupture forces and lower rupture forces, respectively. During experiments using sensitive force probes, it is important that vibrations are not allowed to reach the table top that the equipment is placed on. Usually, this is accomplished by placing the equipment on an anti-vibration table. These tables contain table tops floating on air and are thus decoupled from the vibrations in the building. In the current study, some experiments with OT were performed using a table that due to an unsufficient air pressure was not decoupled from the vibrations in the building. In the following, experimental data achieved both when using and when not using a functioning anti-vibration table are presented.

(a)

(b)
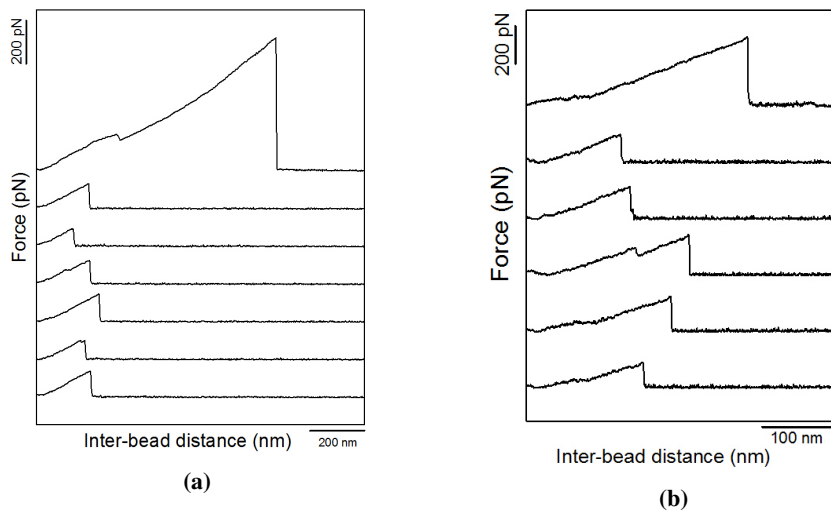
Figure 4.2: Characteristic force vs. inter-bead distance curves with strong rupture forces obtained for the Gal-3 WT - ASF system. (a) Force curves obtained from measurements when using a functioning anti-vibration table. (b) Force curves obtained from measurements when not using a functioning anti-vibration table. The curves were generated from the OT with polystyrene beads functionalized with Gal-3 WT and ASF, respectively.

(a)

(b)
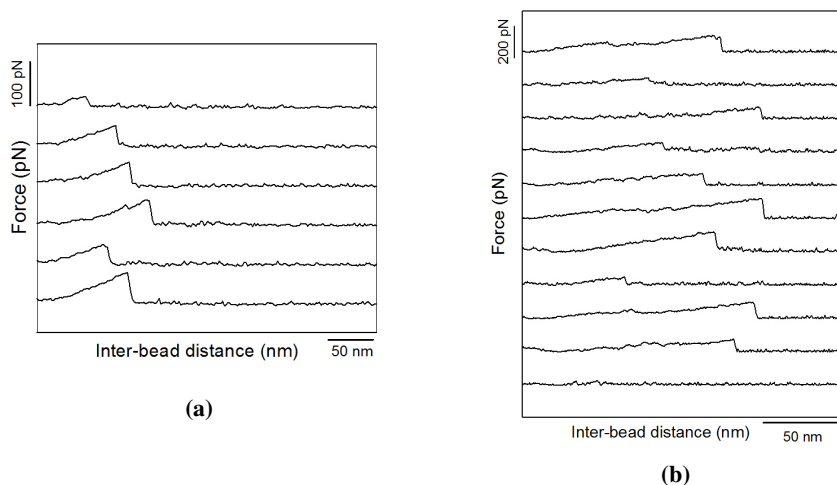
Figure 4.3: Characteristic force vs. inter-bead distance curves containing rupture events of lower force peak obtained for the Gal-3 WT - ASF system. (a) Force curves obtained from measurements when using a functioning anti-vibration table. (b) Force curves obtained from measurements when not using a functioning anti-vibration table. The curves were generated from the OT with polystyrene beads functionalized with Gal-3 WT and ASF, respectively.

4.1.2 Dynamic force spectrum

Figure 4.4 presents the DFS-plot for the Gal-3 WT - ASF system generated from 542 recorded force curves. The data obtained from the system is divided into nine subgroups, and the different colours in the plot indicate the subgroups where the rupture force within a specific loading rate interval are grouped. Figure 4.5 shows the histograms of the distribution of the rupture forces with a corresponding fitted line, P(f), for each subgroup. The different colours in the histograms corresponds to the colours in the DFS-plot. In each histogram is the most likely rupture force, f^*, determined from the fitted line, and the average loading rate of the subgroup, r_f, included. Figure 4.6 shows a separated DFS-plot of the most likely rupture force, f^*, generated from both methods described in Chapter 3, plotted against the average loading rate, r_f. The abrupt alteration of the slope in this plot indicates a transition from one energy barrier to another, in line with the theory presented in Chapter 2. The data in Figure 4.4, Figure 4.5 and Figure 4.6 are based upon the parameters present in the Table 4.1.
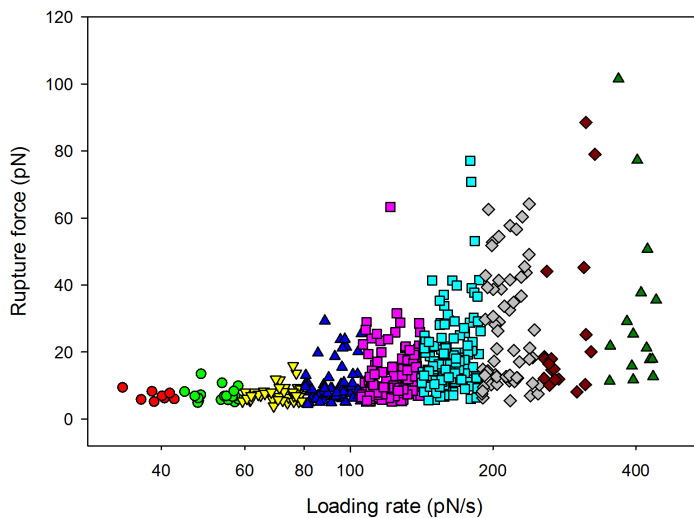
Figure 4.4: Dynamic force spectrum obtained from the interactions between Gal-3 WT and ASF. The plot shows the distribution of the rupture force on the y-axis with increasing loading rate on the logarithmic x-axis. The different colours indicate the subgroups for further histogram analysis. The plot is generated based upon the data in the force curves achieved with OT by polystyrene beads functionalized with Gal-3 WT and ASF, respectively
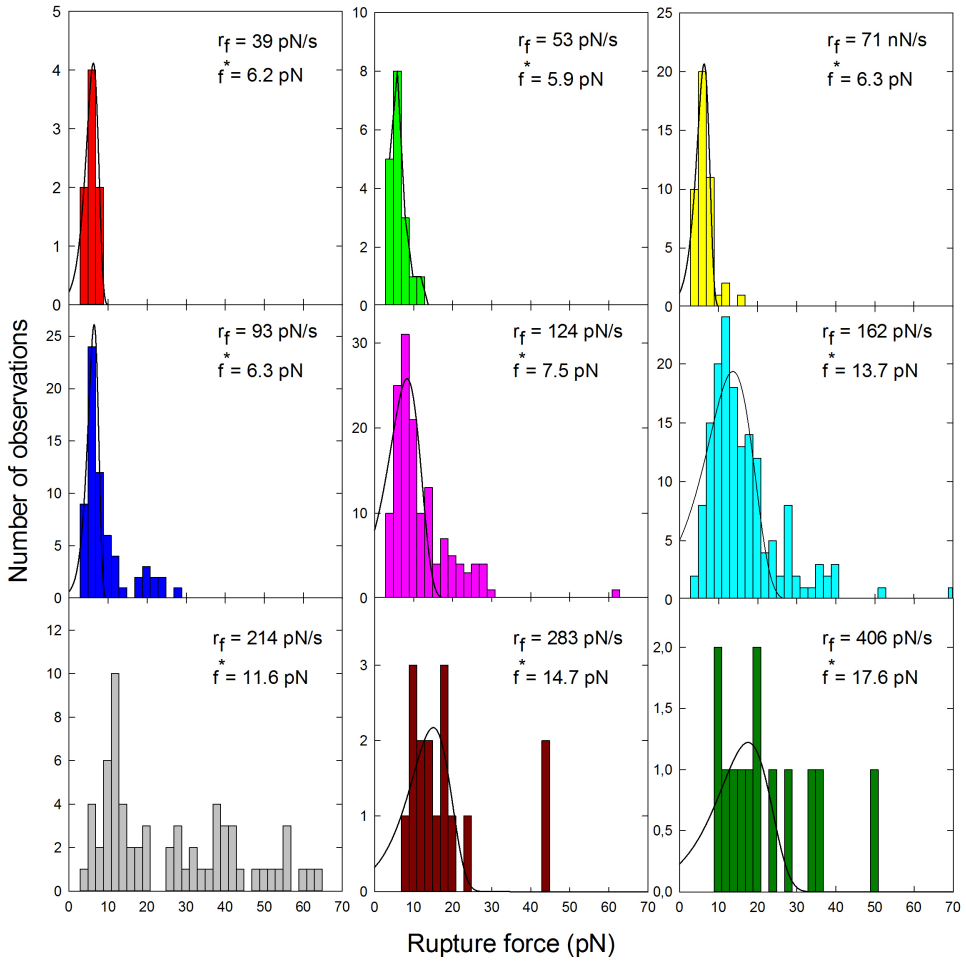
Figure 4.5: Histograms exhibiting the distribution of experimentally determined the inter-molecular rupture forces between Gal-3 WT and ASF. Each histogram is based upon the data for each interval 0 through 8, present in Table 4.1. For each subgroup in the histogram, the most likely rupture force, f*, and the average loading rate, r_f, are included. The fitted distribution of each interval, P(f) (Eq.2.9), is represented by the continuous line. The different colours for each histogram correspond to the defined loading rate interval in the DFS-plot in Figure 4.4. The rupture measurements were obtained from OT by polystyrene beads functionalized with Gal-3 WT and ASF, respectively.
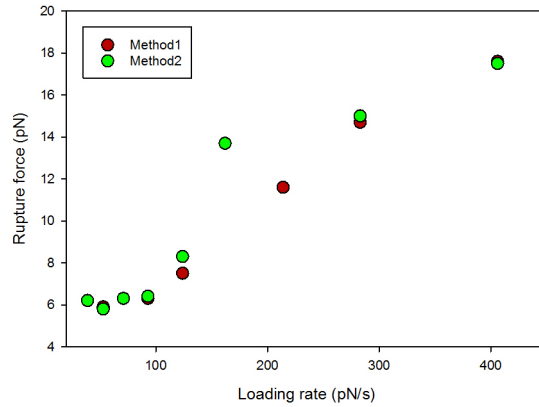
Figure 4.6: The mean value of the most likely rupture force, f^*, and the loading rate, r_f, to each subgroup from figure 4.5 are plotted in a new DFS. The values determined using method 1 and method 2 are displayed in red and green colour, respectively. An abrupt alteration in the slope is observed for loading rates exceeding 100 pN/s, indicating two linear regimes.

4.1.3 Parameters characterizing the interactions between Gal-3 WT and ASF

Based upon the fit of the probability density function, P(f) (Eq. 2.9), to the histograms presented in Figure 4.5, a set of parameters were determined. These parameters describe the energy landscape of the interaction between Gal-3 WT and ASF. Table 4.1 summarize the number of observations for each interval, the average loading rate, r_f, the most likely rupture force, f^*, the estimates of the coefficients dissociation rate, $k_{off,0}$, and the distance between bound and transition state, x_β. Two alternative methods are used to determine f^*, $k_{off,0}$ and x_β, denoted as method 1 and method 2. These different methods are described in Chapter 3, section 3.7. Figure 4.7 shows the x_β-values on the y-axis plotted against the average loading rate, r_f, on the x-axis. Figure 4.8 shows the $k_{off,0}$-values on the y-axis plotted against the average loading rate, r_f, on the x-axis. The x_β- and $k_{off,0}$-values generated from both methods are included. The plots reveal that both x_β and $k_{off,0}$ have two distinct regimes with increasing loading rate, again reflecting the existence of two energy barriers.

Table 4.1: Parameters that characterize the energy landscape of the interaction between Gal-3 WT and ASF: average loading rate (r_f), most likely rupture force (f^*), dissociation rate ($k_{off,0}$), and distance between the bound and transition state (x_β). The parameters f^*, $k_{off,0}$ and x_β are determined by two methods denoted as 1 and 2.

Interval	No. of observations	r_f [pN/s]	f^*,1 [pN]	f^*,2 [pN]	$k_{off,0}$, 1 [1/s]	$k_{off,0}$, 2 [1/s]	x_β, 1 [nm]	x_β, 2 [nm]
0	8	39	6.2	6.2	0.5	0.52	2.53	2.5
1	18	53	5.9	5.8	1.08	0.85	2.31	2.5
2	45	71	6.3	6.3	0.94	0.91	2.47	2.5
3	66	93	6.3	6.4	0.61	1.18	2.98	2.5
4	143	124	7.5	8.3	3.96	6.03	0.99	0.6
5	160	162	13.7	13.7	2.83	3.17	0.66	0.6
6	65	214	11.6	-0.45	6.05	5.63	0.06	0.6
7	18	283	14.7	15.0	3.11	4.72	0.77	0.6
8	19	406	17.6	17.5	4.47	4.42	0.60	0.6
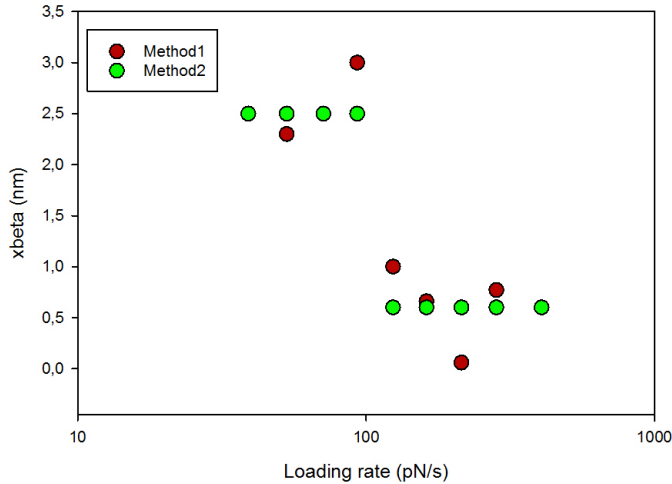
Figure 4.7: Distance from bound to transition state, x_β, for each interval, on the y-axis with increasing loading rate on the x-axis. The red colour present values determined by method 1, and the green colour present values determined by method 2. The results reveal that there are a transition from one energy barrier at loading rates up to $\sim$100 pN/s, to another energy barrier at loading rates beyond 100 pN/s.
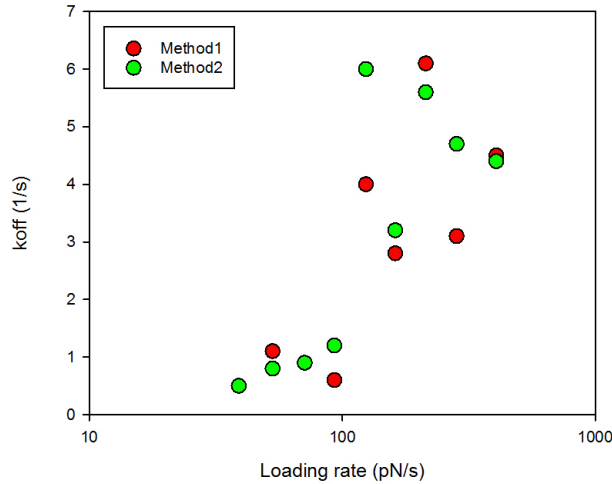
Figure 4.8: Dissociation rate, $k_{off,0}$, for each interval, on the y-axis with increasing loading rate on the x-axis. The red colour present values determined by method 1, and the green colour present values determined by method 2. The results reveal that there are a transition from one energy barrier at loading rates up to $\sim$100 pN/s, to another energy barrier at loading rates beyond 100 pN/s.

4.2 Experimental data for Gal-3 homodimer - ASF interactions

In this part of the study, the substrate binding abilities of Gal-3 homodimer were investigated by using ASF as a substrate. By analyzing the data achieved from the OT retraction experiments it was possible to generate galleries of the force curves, DFS-plot and the parameters describing the interaction between Gal-3 homodimer and ASF. In the following section, the experimental data obtained from the interactions between Gal-3 homodimer and ASF is presented. The new data obtained in the current study builds on the previous data obtained by Sylvi Oliva Kjær (Kjær, 2018).

4.2.1 Galleries

Figure 4.9 presents a selection of typical force curves obtained from the Gal-3 homodimer - ASF system. Significantly higher rupture forces were observed for the system, shown in

Figure 4.10a, as well as rupture events with lower forces, displayed in Figure 4.10b.
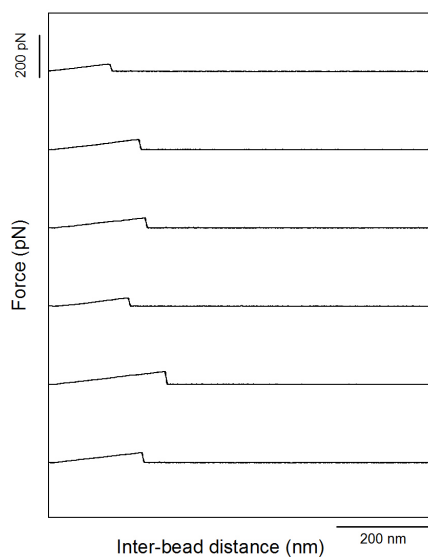
Figure 4.9: A selection of typically observed force vs. inter-bead distance curves for rupture events obtained from the Gal-3 homodimer - ASF system. The curves were generated from the OT with polystyrene beads functionalized with Gal-3 homodimer and ASF, respectively.

(a) Strong rupture force curves

(b) Weak rupture force curves
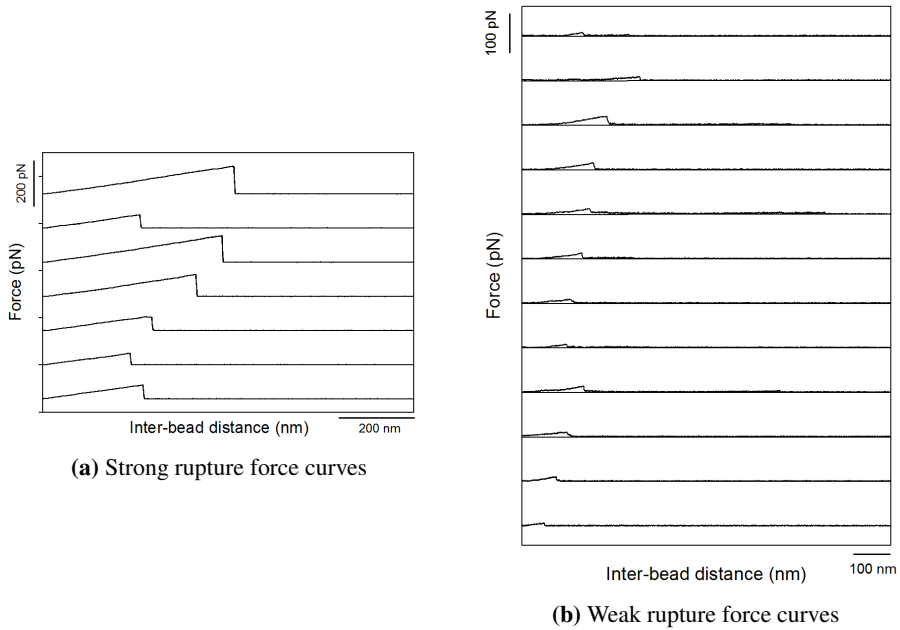
Figure 4.10: A selection of force vs. inter-bead distance curves obtained from the Gal-3 homodimer - ASF system. (a) Force curves with high rupture forces. (b) Force curves with low rupture forces. The curves were generated from the OT with polystyrene beads functionalized with Gal-3 homodimer and ASF, respectively.

4.2.2 Dynamic force spectrum

Figure 4.11 presents the DFS-plot for the Gal-3 homodimer - ASF system generated from 841 recorded force curves. The data obtained from the system is divided into nine subgroups and the different colours in the plot indicate the subgroups where the rupture force within a specific loading rate interval are grouped. Figure 4.12 shows the histograms of the distribution of the rupture forces with a corresponding fitted line, P(f), for each subgroup. The different colours in the histograms corresponds to the colours in the DFS-plot. In each histogram is the most likely rupture force, f^*, determined from the fitted line, and the average loading rate of the subgroup, r_f, included. Figure 4.6 presents a plot of the most likely rupture force, f^*, generated from both methods, and the average loading rate, r_f, for each subgroup in the histogram. This plot indicates two slopes, hence reflecting the existence of two energy barriers. The data in Figure 4.11, Figure 4.12 and Figure 4.13 are based upon the parameters present in the Table 4.2.
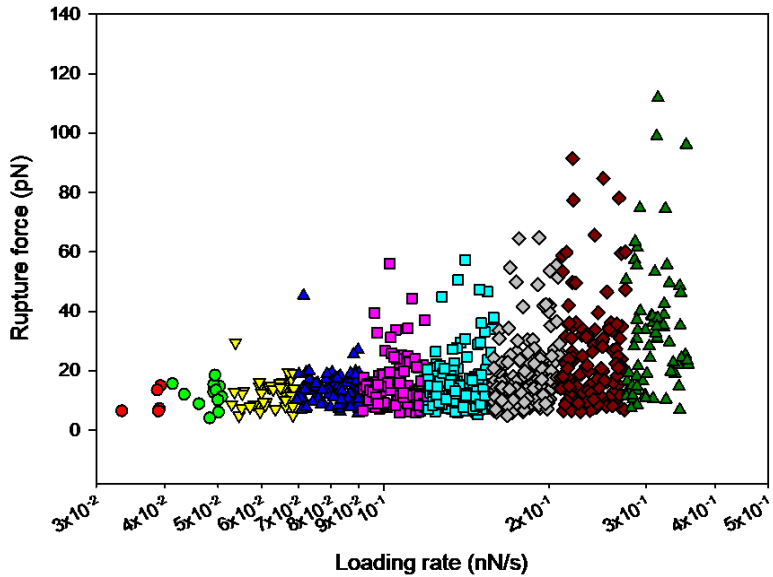
Figure 4.11: Dynamic force spectrum obtained from the interactions between Gal-3 homodimer and ASF. The plot shows the distribution of the rupture force on the y-axis with increasing loading rate on the logarithmic x-axis. The different colours indicate the subgroups for further histogram analysis. The plot is generated based upon the data in the force curves achieved with OT by polystyrene beads functionalized with Gal-3 homodimer and ASF, respectively
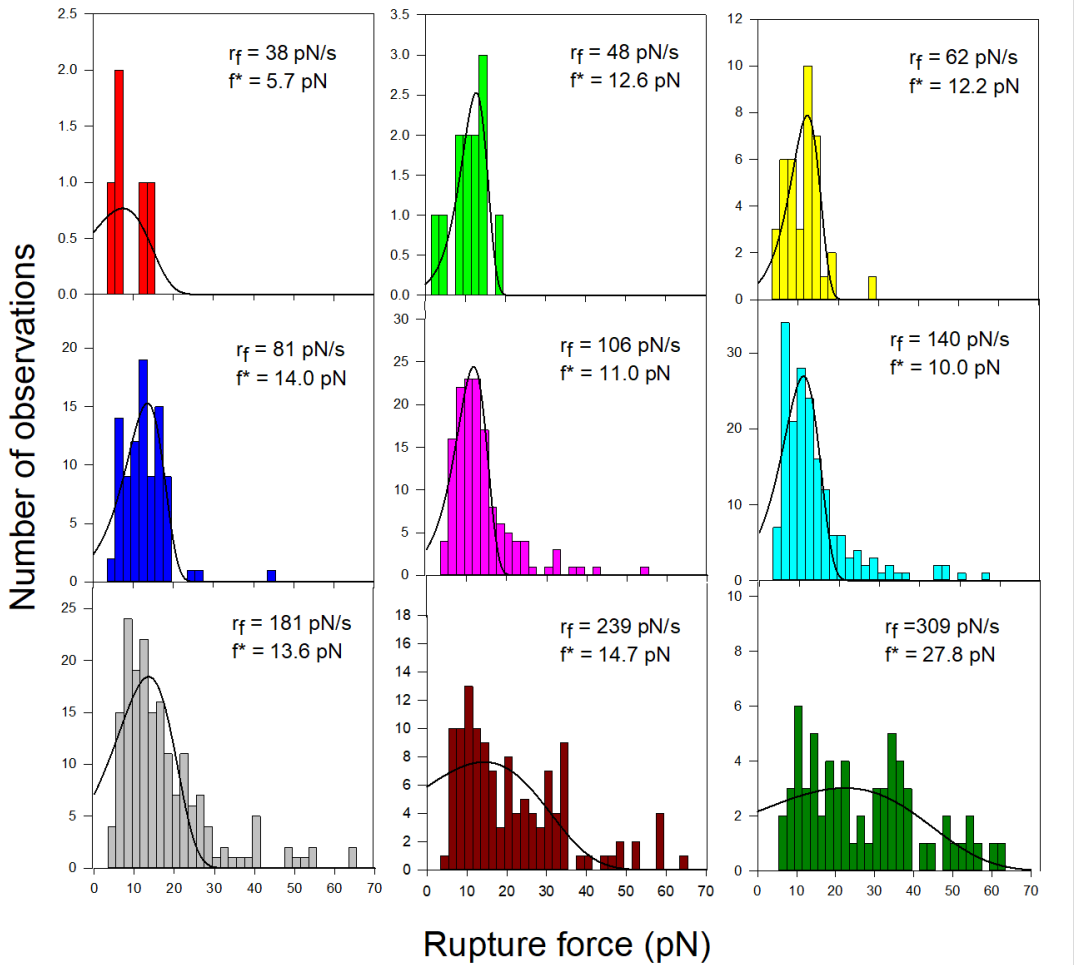
Figure 4.12: Histograms exhibiting the distribution of experimentally determined the inter-molecular rupture forces between Gal-3 homodimer and ASF. Each histogram is based upon the data for each interval 0 through 8, present in Table 4.2. For each subgroup in the histogram, the most likely rupture force, f*, and the average loading rate, r_f, are included. The fitted distribution of each interval, P(f) (Eq.2.9), is represented by the continuous line. The different colours for each histogram correspond to the defined loading rate interval in the DFS-plot in Figure 4.11. The rupture measurements were obtained from OT by polystyrene beads functionalized with Gal-3 homodimer and ASF, respectively.
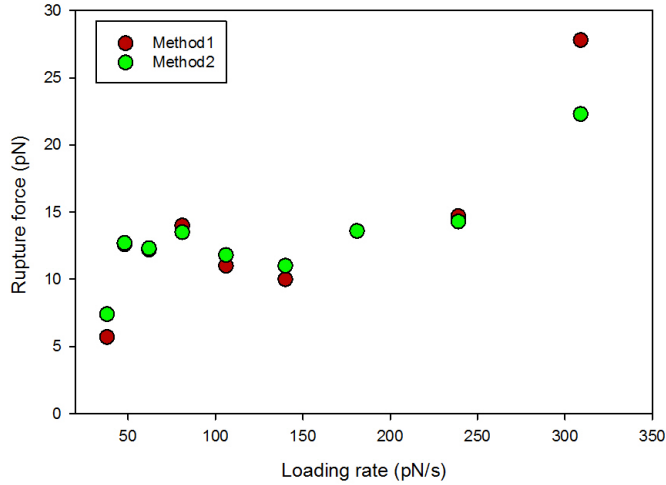
Figure 4.13: The mean value of the most likely rupture force, f^*, and loading rate, r_f, to each subgroup from figure 4.12 are plotted in a new DFS. The values determined using method 1 and method 2 are displayed in red and green colour, respectively. An abrupt alteration in the slope is observed for loading rates exceeding 100 pN/s, indicating two linear regimes.

4.2.3 Parameters characterizing the interactions between Gal-3 homodimer and ASF

Based upon the fit of the probability density function, P(f) (Eq. 2.9), to the histograms presented in Figure 4.12, a set of parameters were determined. These parameters describe the energy landscape of the interaction between Gal-3 homodimer and ASF. Table 4.2 summarizes the number of observations for each interval, the average loading rate, r_f, the most likely rupture force, f^*, the estimates of the coefficients dissociation rate, $k_{off,0}$, and the distance between bound and transition state, x_β. As before, two alternative methods are used to determine f^*, $k_{off,0}$ and x_β, denoted as method 1 and method 2. Figure 4.14 shows the x_β-values on the y-axis plotted against the average loading rate, r_f, on the x-axis. Figure 4.15 shows the $k_{off,0}$-values on the y-axis plotted against the average loading rate, r_f, on the x-axis. The x_β- and $k_{off,0}$-values generated from both methods are included. The plots reveal that both x_β and $k_{off,0}$ are assembled in two distinct regimes with increasing loading rate.

Table 4.2: Parameters that characterize the energy landscape of the interaction between Gal-3 homodimer and ASF: average loading rate (r_f), most likely rupture force (f^*), dissociation rate ($k_{off,0}$), and distance between the bound and transition state (x_β). f^*, $k_{off,0}$ and x_β are determined by two methods denoted as 1 and 2.

Interval	No. of observations	r_f [pN/s]	f^*,1 [pN]	f^*,2 [pN]	$k_{off,0}$, 1 [1/s]	$k_{off,0}$, 2 [1/s]	x_β, 1 [nm]	x_β, 2 [nm]
0	5	38	5.7	7.4	1.89	2.19	0.52	1.11
1	12	48	12.6	12.7	0.31	0.42	1.24	1.11
2	39	62	12.2	12.3	0.59	0.59	1.11	1.11
3	92	81	14.0	13.5	1.02	0.48	0.84	1.11
4	141	106	11.0	11.8	1.32	3.47	1.04	0.45
5	177	140	10.0	11.0	2.84	5.12	0.86	0.45
6	180	181	13.6	13.6	4.0	4.42	0.53	0.45
7	125	239	14.7	14.3	6.03	5.16	0.23	0.45
8	70	309	27.8	22.3	5.09	1.58	0.17	0.45
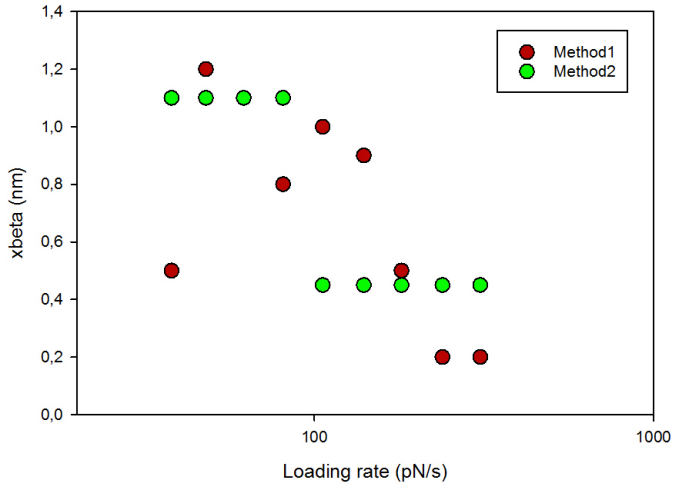
Figure 4.14: Distance from bound to transition state, x_β, for each interval, on the y-axis with increasing loading rate on the x-axis. The red colour present values determined by method 1, and the green colour present values determined by method 2. The results display that the x_β-values are assembled in two regimes, indicating a transition from one energy barrier to another energy barrier at increasing loading rate.
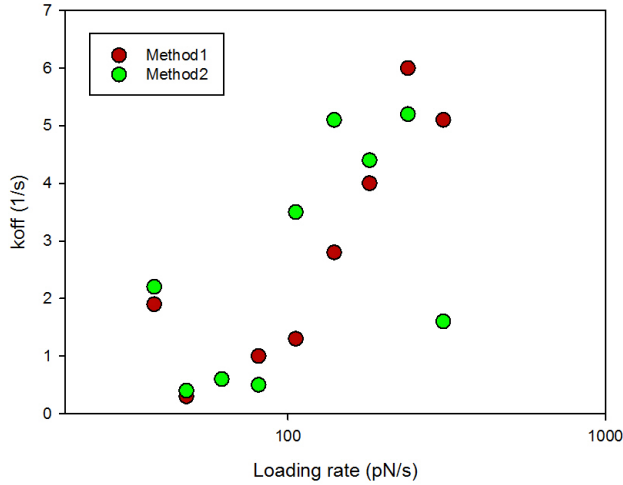
Figure 4.15: Dissociation rate, $k_{off,0}$, for each interval, on the y-axis with increasing loading rate on the x-axis. The red colour present values determined by method 1, and the green colour present values determined by method 2. The results display that the $k_{off,0}$-values are assembled in two regimes, indicating a transition from one energy barrier to another energy barrier at increasing loading rate.

4.3 Comparison of the galectins: Gal-3 WT and Gal-3 homodimer

This section presents the experimental data obtained throughout the whole experiment to facilitate the comparison between the two systems investigated: Gal-3 WT- ASF and Gal-3 homodimer - ASF. Table 4.3 summarizes the average values of the dissociation rate, $\overline{k_{off,0}}$, the distance between bound and transition state, $\overline{x_\beta}$, and the lifetime, $\overline{\tau}$, determined from the intervals with lower loading rates. The outliers observed in interval 0 for the Gal-3 homodimer - ASF system are neglected when calculating the mean value. To obtain a clearer representation of the comparison of the DFS-plots, the most likely rupture forces are plotted against the increasing loading rate for both of the systems in Figure 4.16. A combined representation of distance between bound and transition state, x_β, and the dissociation rate, $k_{off,0}$, for both systems are plotted as a function of increasing loading rate in Figure 4.17 and Figure 4.8, respectively. The data in Table 4.3, Figure 4.16, Figure 4.17 and Figure 4.18 are all based upon the parameters present in Table 4.1 and Table 4.2.

Table 4.3: Summary of the average parameter values obtained by the lower range of loading rates (up to ~ 100 pN/s): dissociation rate ($\overline{k_{\text{off},0}}$), lifetime ($\overline{\tau}$) and distance from bound to transition state ($\overline{x_\beta}$) for both of the systems with the associated standard deviation. The values are calculated from the data yielded in Table 4.1 and 4.2 and τ is calculated from Eq. 2.6. The outlier observed in interval number 0 for the Gal-3 homodimer - ASF system is neglected when calculating the mean values of this system.

System	$\overline{k_{\text{off},0}}$ [1/s]	$\overline{\tau}$ [s]	$\overline{x_\beta}$ [nm]
Gal-3 WT - ASF	0.78 ±0.27	1.4±0.5	2.57±0.29
Gal-3 homo - ASF	0.64±0.36	1.97±1.15	1.06±0.2
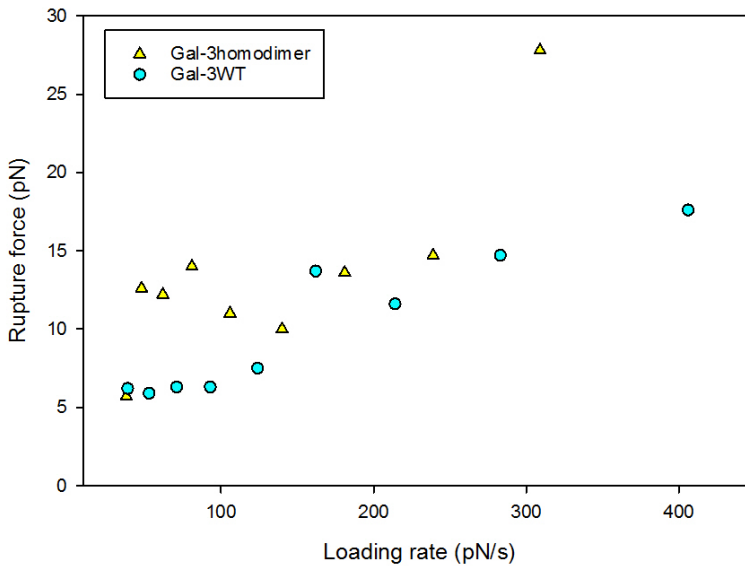
Figure 4.16: A combined dynamic force spectrum for the two systems: Gal-3 WT - ASF and Gal-3 homodimer - ASF, obtained from the most likely rupture forces, f*, from the fit P(f) (Eq. 2.9) to the histograms in Figure 4.5 and Figure 4.12, plotted against the increasing loading rate, r_f.
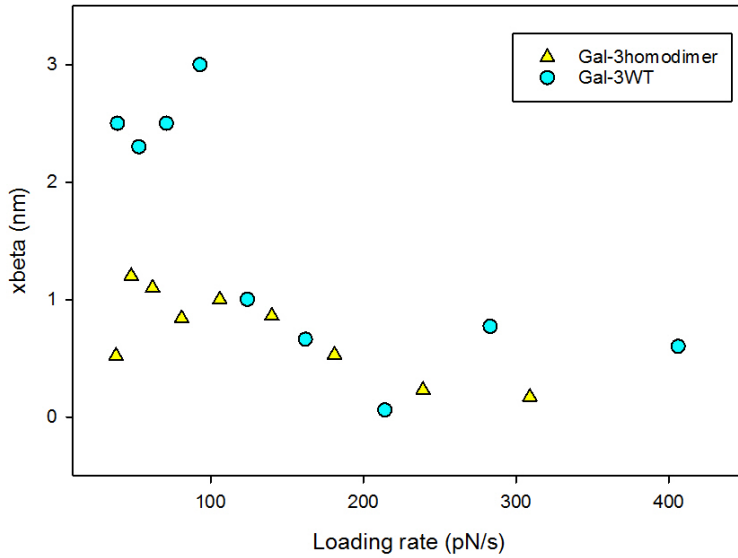
Figure 4.17: A combined representation of the x_β-values for the two systems: Gal-3 WT - ASF and Gal-3 homodimer - ASF, obtained from the parameters present in Table 4.1 and Table 4.2, plotted as a function of increasing loading rate, r_f.
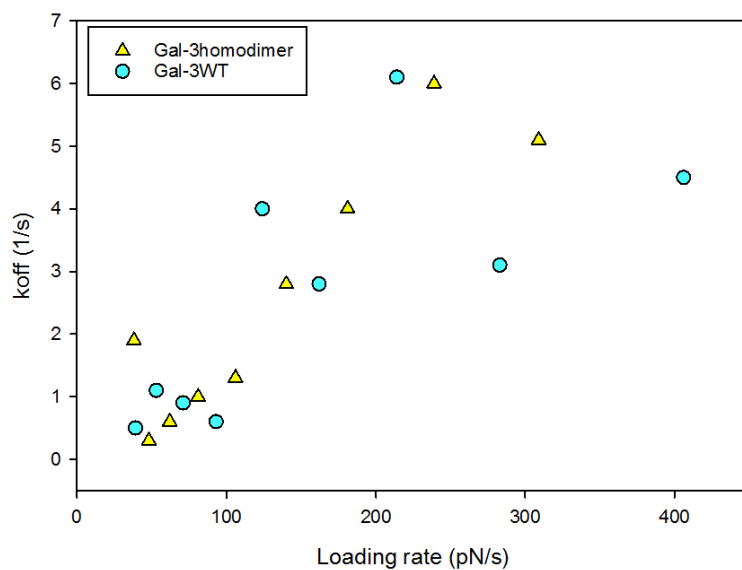
Figure 4.18: A combined representation of the $k_{off,0}$-values for the two systems: Gal-3 WT - ASF and Gal-3 homodimer - ASF, obtained from the parameters present in Table 4.1 and Table 4.2, plotted as a function of increasing loading rate, r_f.

Chapter 5

Discussion

The following chapter gives a thorough examination of the results presented in Chapter 4. In the first part, the application of OT as a tool to study glycan-lectin interactions is evaluated. In the second part, the interaction events of the two systems are discussed based on the force-distance curves. The next part discusses the differences observed in the experimental data for the Gal-3 WT - ASF system obtained from the previous study and the present study. Further, the information extracted from the DFS analysis is discussed. Finally, the differences between the interaction abilities of the two systems studied are discussed, also in light of their respective structures.

5.1 The application of OT to study lectin - glycan interactions

The emergence of single-molecule spectroscopy techniques has opened up the opportunity to investigate biological processes regulated by force, such as weak inter-molecular interactions. All three techniques presented in Chapter 2, Section 2.2 are suitable tools to study lectin-glycan interactions in the single molecular level, like those investigated in the current study (Neuman and Nagy, 2008). Further, OT is, since it provides a high force and time resolution also in this range, the preferred method when investigating forces in the low power range. Accordingly, OT is considered a powerful tool to quantify the single molecular interaction forces that were of interest in the current study.

5.2   Interaction events quantified by OT

Figure 4.2, 4.3, 4.9 and 4.10 show force vs. inter-bead distance curves obtained from OT measurements for each system. These curves indicate that interactions between the glycoprotein ASF and the two different structural forms of Gal-3 occur. This conclusion is consistent with previous findings (Dam et al. (2005), Kjær (2018), Wik (2019)). The curves display a sudden rise in force leading to an evident peak, indicating the bond breakage. The slope given by the rise in force per unit time reflects the increasing force that the bond is exposed to when the beads are pulled apart, giving rise to the force jumps recorded by OT.

However, during some of the experiments between Gal-3 WT and ASF, experimental noise, in form of vibrations, was observed in the corresponding force curves (Figure 4.2b and 4.3b). As described in Materials and Methods, Section 3.4, this factor was minimized by placing the instrument on a vibration isolated table. During some of the measurements, the table was not properly adjusted which gave rise to the experimental noise in the recorded force curves. Despite that, there was good correspondence between the datapoints (Figure 4.4) obtained under conditions of high or low noise level, indicating that the noise did not affect the determination of rupture forces and loading rates.

The force vs. inter-bead distance curves presented in the galleries in Chapter 4, indicating contrasts in the rupture force sizes for both systems. Figure 4.2 and 4.10a show rupture events implying significantly higher rupture forces compared to the events presented in Figure 4.3 and 4.10b. However, as displayed in the DFS-plot for both systems (Figure 4.4 and 4.11), the incidence of these high rupture forces are low.

5.3   Comparison with previous research of the Gal-3 WT - ASF system and multivalency

The interaction abilities between Gal-3 WT and ASF have previously been investigated in Kjær's master thesis utilizing the same methods as in the present study. Figure 4.1 demonstrates that the results from the current study obtained higher loading rate levels at similar rupture force levels compared to the previous study. Friddle et al. (2012) showed in their study that the loading rate at the same level of rupture forces decreases with increasing number of parallel individual bonds for the avidin-biotin system. Accordingly, the rise in loading rate level obtained in the present study can reflect a lower amount of multiple

interactions, as the data from Kjær's thesis displayed a high frequency of multiplicity in the system.
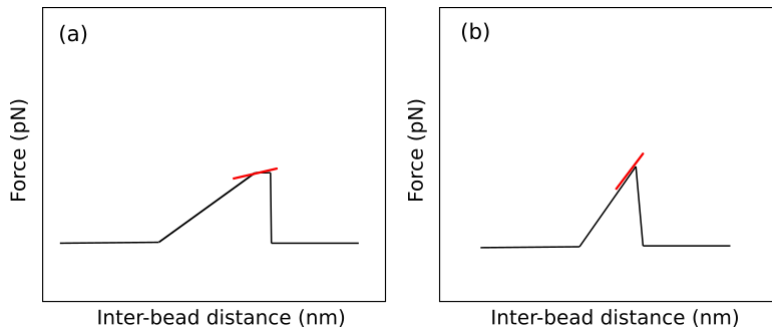
Figure 5.1: Simple illustration of the different rupture events, with rupture force (pN) plotted against inter-bead distance (nm). The red coloured lines show the fitted loading rate for each of the events. (a) Shows the scenario of a slower increase in the force prior to rupture providing lower loading rate. (b) Presents the scenario of a steeper slope towards the peak force providing higher loading rate

Figure 5.1 shows a simplified illustration of force plotted against inter-bead distance for two scenarios with different rupture events. The loading rates, indicated in red, are generated from the slope of the force curve prior to bond rupture. Figure 5.1a displays the scenario of a slower slope towards the peak force, providing a low loading rate, and occasionally a negative increase in force. Such force curves generated by OT have been observed in previous studies and have been identified to be a result of multiple bonds rupturing (Hadjialirezaei et al. (2017), Haug (2017)). Whereas, Figure 5.1b shows an example of a force curve with a steeper slope towards the peak force, yielding higher loading rate and indicating a single rupture event.

The fact that Gal-3 monomers have the potential to form pentamer structures, as mentioned in Section 2.1.1, increases the possibility of multivalency. In addition, ASF possesses several epitopes that Gal-3 can interact with, increasing the potential of multiple interactions. If aiming to quantify monovalent interactions, a low probability of observing rupture events is crucial, because that ensures the rupture of single molecular bonds (Evans, 1999). Accordingly, it is essential to have a low concentration of molecules on the bead surface. In the present study, there were low occurrences of interaction events during the measurements, implying that single molecular bonds were ruptured between Gal-3 WT and ASF. This assumption is also in accordance with the higher loading rate levels observed in the obtained experimental data. Although, this is more time consuming

as the probability of rupture events reduces.

5.4 The energy landscape of the two systems studied

For both systems, the total number rupture events were identified and utilized to determine the most likely rupture force, f^*, and the average loading rate, r_f. Figure 4.4 and 4.11 present the DFS-plot for the Gal-3 WT and Gal-3 homodimer interactions with ASF, respectively. For both systems the observations were divided into nine subgroups along the axis of increasing loading rate. These observations display a trend of increasing rupture forces with increasing loading rates, corresponding to the theory (Evans and Ritchie, 1997). The associated histograms are presented in Figure 4.5 and 4.12, including the fitted distribution. By fitting Eq. 2.9 to the experimental data, the estimates of x_β, $k_{off,0}$ and τ were obtained from both interactions (Table 4.1 and 4.2). These parameters yield information about the shape of the energy landscape and lifetime of the inter-molecular interactions.

5.4.1 Energy landscape of the Gal-3 WT - ASF system

For the Gal-3 WT - ASF system, the most likely rupture forces, f^*, range from 6.2 pN to 17.6 pN for loading rates between 39 pN/s and 406 pN/s. All the intervals in Figure 4.5 have a fitted distribution based upon Eq. 2.9, with the exception of interval number 6. Based on the obtained data it was possible to determine the different parameters describing the energy landscape.

Figure 4.6 shows a slight increase of the most likely rupture force, f^*, from 6.2 pN to 6.3 pN, with increasing loading rates, r_f, up to about 100 pN/s. Followed by a transition to a more rapid increase of f^*, from 7.5 pN to 17.6 pN, with increasing loading rates beyond 100 pN/s. This reveals that two prominent energy barriers exist along the unbinding pathway (Evans, 1999), as illustrated in Figure 2.11. The transition from one linear regime to another corresponds to a change of slope yielding a new linear regime, and thus indicating a crossover between the energy barriers has occurred. Also, there is a correlation between the most likely rupture force, f^*, determined from both methods, which indicate consistency between the two methods.

In Table 4.1 are the results of the location of the energy barriers, x_β, presented. The results indicate that two values of x_β exist along the unbinding pathway, hence revealing

the presence of two energy barriers. Additionally, Figure 4.7 displays that the x_β-values alter around 100 pN/s. Based on the first four intervals the x_β is ranging between 2.31 nm and 2.98 nm, yielding an average x_β-estimate of 2.57±0.29 nm. This demonstrates the position of the outer barrier. Whereas, for the last five intervals x_β is ranging between 0.06 nm and 0.99 nm, providing an average x_β-estimate of 0.62±0.34 nm, which describes the position of the inner barrier.

An alternative approach to estimate the x_β-values is based on the slope of the linear regimes in Figure 4.6. This slope is defined as $\frac{k_B T}{x_\beta}$, and states the position of the barriers located along the direction of applied force (Evans, 1999). In Table 4.1 (last column) are the x_β-estimates determined by this approach presented. By using this method, the position of the outer barrier is determined to x_β = 2.5 nm, while the position of the inner barrier is determined to x_β = 0.6 nm. The remarkable correspondence between the values determined using the two different approaches provides credibility to the experimental data. In addition, these results are comparable with values obtained from previous studies for other ligand-receptor interactions: Håti et al. (2015) found x_β for the inner barrier and the outer barrier in the interval 0.2-0.5 nm and 1.5-3.5 nm, respectively, for the AlgE4 and AlgE6-poly-M complexes. Stangner et al. (2013) found x_β equal to 0.54 nm for the interaction between monoclonal antibody HPT-101 and tau-peptide, and Burgos-Bravo et al. (2018) estimated a x_β equal to 0.50 nm for the Thy-1 - αvβ3-integrin interaction.

Figure 4.8 also reveals that two different regimes of $k_{off,0}$ exist along increasing loading rates, which is in accordance with the presence of two energy barriers. The values of $k_{off,0}$ achieved by fitting the parameters in Eq. 2.9 to the distributions of the experimentally rupture forces are presented in Table 4.1. For the observations assembled for loading rates up to 100 pN/s, $k_{off,0}$ range from 0.5 s^{-1} to 1.08 s^{-1}, yielding an average value of $k_{off,0}$ equals to 0.78±0.27 s^{-1}. For the loading rates beyond 100 pN/s the values obtained are more scattered, reflecting challenges with determining these values with high accuracy. For this range of loading rates, $k_{off,0}$ ranges between 2.83 s^{-1} and 6.05 s^{-1}, which provide an average of $k_{off,0}$ equals to 4.08±1.28 s^{-1}. This indicate that $k_{off,0}$ increases with increasing loading rates which is expected because the Bell-Evans model predicts that the dissociation rate increases exponentially with force, as described in Eq. 2.5 (Evans, 1999). Further, the lifetime, τ, is found by using Eq. 2.6. This provides a lifetime equal to 0.26±0.08 s and 1.4±0.5 s for the inner and outer barrier, respectively. The values of $k_{off,0}$ were also obtained from the alternative approach, providing a mean value of $k_{off,0}$ = 0.87±0.27 s^{-1} for the lower range of loading rates, and $k_{off,0}$ = 4.79±1.12 s^{-1} for the higher range of loading rates. Despite the challenges associated with an accurate determination of $k_{off,0}$ in the high loading rate regime, the consistency between the data extracted

from both methods adds credibility to the obtained experimental data.

According to Kjær's thesis (Kjær, 2018), it was difficult to draw a conclusion based upon the estimate of x_β and $k_{off,0}$ for the Gal-3 WT - ASF system, due to high uncertainty. However, adding new data of the Gal-3 WT and ASF system provided a clearer indication of the existence of two energy barriers. The presence of multiple barriers often appears when unbinding processes are investigated in a wider range of loading rates (Bizzarri and Cannistraro, 2010).

5.4.2 Energy landscape of the Gal-3 homodimer - ASF system

The results reveal that the most likely rupture force, f^*, range from 5.7 pN to 27.8 pN for increased average loading rates between 38 pN/s and 309 pN/s for the Gal-3 homodimer - ASF system. Figure 4.13 demonstrates that there is a high correspondence between the rupture forces and loading rates extracted from the two different methods.

Before looking into the parameters in Table 4.2, it is to be noted that the outliers observed in interval 0 for both x_β- and $k_{off,0}$-value were neglected when calculating the mean value, due to high variance compared to the other obtained values. It is reasonable to assume this could be a result of a low number of observations in the interval 0.

The parameters describing the energy landscape reveals the existence of two energy barriers, with a crossover also around 100 pN/s. The intervals in the lower range of loading rates (below 100 pN/s) have x_β-values ranging from 0.84 nm to 1.24 nm, yielding a mean value equal to 1.06±0.2 nm. This number describes the distance separating the location of the outer energy barrier from the binding site. The last five intervals situated at higher loading rates, have x_β-values that range from 0.17 nm to 1.04 nm, providing a mean value equal to 0.57±0.38 nm, indicating the inner energy barrier. In addition, in Table 4.2 (last column), the x_β-values determined from the other approach are presented, yielding an estimate of $x_\beta = 1.11$ nm and $x_\beta = 0.45$ nm for the outer and the inner energy barrier, respectively. In Figure 4.14, the x_β-values determined from both methods are plotted against increasing loading rates, showing that the x_β-values are situated in two regimes. However, there are high variations between some of the values generated from the two different methods.

For the lower range of loading rates, the values of $k_{off,0}$ are ranging from 0.31 s^{-1} to 1.02 s^{-1}, with a mean dissociation rate equals to 0.64±0.36 s^{-1}, that corresponds to a lifetime, τ, of 1.97±1.15 s. In the high loading rate regime, the $k_{off,0}$-values are more scattered and vary from 1.32 s^{-1} and 6.02 s^{-1}, yielding a mean value equal to 3.85±1.85 s^{-1} and a lifetime, τ, of 0.34±0.24 s. Thus, the determination of accurate values are challenging in

this regime. As for the other approach, $k_{off,0}$-values were determined to be $3.95\pm1.49\text{ s}^{-1}$ and $0.5\pm0.09\text{ s}^{-1}$, for the inner and outer barrier, respectively. In Figure 4.15 are the $k_{off,0}$-values generated from both methods plotted together with increasing loading rates. This indicates that $k_{off,0}$ exists in two regimes when the loading rate increases. However, there are also variations between some of the determined values of $k_{off,0}$ from both approaches, particularly for the higher loading rate regime. This provide uncertainty to the obtained parameters and will be discussed in the next section.

The parameters obtained in this study are in accordance with other glycan-lectin studies using OT, thus providing credibility to the results obtained. In the study conducted by Hadjialirezaei et al. (2017) for MUC1(Tn) - MGL system, the interaction strength (f^*) was found to range from 6.8 pN to 27 pN for loading rates of 29 - 135 pN/s, $k_{off,0}$ from 1.5 s^{-1} to 2.3 s^{-1}, and x_{β}-values in the range from 0.12 nm to 0.51 nm. The same study found $\tau = 0.3$ s for the inner barrier in the MGL - MUC1(STn) system.

5.4.3 Uncertainty in the parameters characterizing the energy landscape

To obtain robust estimates of the parameters characterizing the energy landscape there should be a large set of data. This will provide more accurate parameters. However, as mentioned in the the theory section 2.3, because of the stochastic nature of the system, a variation between the parameters determined is expected (Håti et al., 2015). Thus, to attain higher certainty in the parameters characterizing the energy landscape, more observations will be beneficial.

Additionally, the multivalent nature of both galectins could be an explanation to the variation in the data. As discussed in the previous section, Gal-3 WT has the ability to form pentamers which can result in multiple interactions. Furthermore, as described in Chapter 2, Section 2.1.1, Gal-3 homodimer consists of two CRDs that can give rise to multiple interactions with the ligand depending on the orientation of the molecule. By using the immobilization procedure outlined in Chapter 3, it is not achievable to control the orientation of the immobilized proteins on the beads. Accordingly, the CRDs of the homodimer can be orientated in two ways: the CRDs are pointing in the opposite direction enabling only one of the CRDs to interact with the ligand, or the CRDs are pointing in the same direction allowing both CRDs to interact with the ligand. Consequently, the latter orientation of the molecule may give rise to multiple interactions. In addition, it is difficult to determine if several monomers of Gal-3 WT are assembled to pentamers based on the immobilization

procedure. Moreover, as described in Section 2.1.2, the ASF molecule expresses several epitopes, where each has the ability to interact with the galectins. This also increases the probability of multiple interactions events.

For further studies, it can be of interest to implement other methods for DFS analysis in order to obtain even more accurate parameters. In the present study, the results are based upon the Bell-Evans model. As mentioned in the theory section 2.3, the Bell-Evans model assumes that the unbinding force is irreversible and the rebinding process is neglected, leading to a linear fit between the most probable rupture force and the logarithm of loading rate. Dudko et al. (Dudko et al. (2008), Hummer and Szabo (2003)) extended this model by adding a new parameter representing the geometry of the energy landscape and suggesting a new method for determining τ. Further, Friddle et al. (Friddle et al., 2012) have proposed a novel approach of interpreting the force data by taking the rebinding process into account. This model introduces two distinct regimes during molecular unbinding: a near-equilibrium regime at low loading rates where the molecules can rebind, and a kinetic phase at sufficiently higher loading rates where unbinding is irreversible. Resulting in a nonlinear manner of the mean rupture force and the logarithm of loading rate.

5.5 Comparison of the interaction abilities between the two systems studied: Gal-3 WT - ASF and Gal-3 homodimer - ASF

Dynamic force measurements of the rupture forces in the two investigated systems reveal that two energy barriers exist along the unbinding process with a transition from one energy barrier to another at loading rate around 100 pN/s, for both systems. For the Gal-3 WT - ASF system, the rupture forces range between 6.2 pN and 17.6 pN for loading rates between 39 pN/s and 406 pN/s. Whereas, the rupture forces range between 5.7 pN and 27.8 pN for loading rates between 38 pN/s and 309 pN/s for the Gal-3 homodimer - ASF system (Table 4.1, 4.2).

Figure 4.16 shows the most likely rupture force, f*, plotted against the increasing average loading rate, r_f, for both systems. Based upon the lower range of loading rates (up to about 100 pN/s) in Figure 4.16, the results reveal that the Gal-3 homodimer yields higher rupture forces compared to Gal-3 WT. This suggests that, at low loading rate, Gal-3 homodimer exerts stronger interactions with the glycoprotein ASF than what Gal-3 WT does. For the high loading rates (above $\sim$ 100 pN/s), the comparison between the systems is more

complicated as there is more variation in the data.

Figure 4.18 presents the $k_{off,0}$-values with increasing loading rates for both systems. The average $\overline{k_{off,0}}$- values was found to be 0.78±0.27 s^{-1} for the Gal-3 WT - ASF system, and 0.64±0.36 s^{-1} for the Gal-3 homodimer - ASF system. These values correspond to average lifetimes equal to 1.4±0.5 s and 1.97±1.15 s, respectively (Table 4.3). Still, the outlier in interval number 0 for the Gal-3 homodimer - ASF system was neglected when calculating the mean values. The results suggest that bonds forming between Gal-3 homodimer and ASF have a longer lifetime compared to Gal-3 WT, reflecting the stronger interaction that the homodimer exerts. The same tendency was displayed in the study by Håti et al. (2015), where the AlgE4 - PolyM system showed the strongest interaction as well as the longest lifetime relative to the other systems studied.

Figure 4.17 presents the x_β-values with increasing loading rates for both systems, also showing a clear difference at lower loading rates. The $\overline{x_\beta}$-values presented in Table 4.3 displays that Gal-3 WT exhibits a higher $\overline{x_\beta}$-value with more than twofold the distance of the homodimer system, with an average value of 2.57±0.29 nm. Whereas, $\overline{x_\beta}$ = 1.06±0.2 nm for the Gal-3 homodimer system, indicating a shorter separation distance between the Gal-3 homodimer and ASF when bound to each other. These findings indicate that the homodimer system exhibits a stronger interaction with longer lifetime and shorter separation distance at the regime of lower loading rate.

5.5.1 Comparison of the findings based upon the structural differences between the galectins

The disparities in the data set comparison presented in Section 4.3 can be explained by the structural differences between the two galectins. Figure 2.3 and Figure 2.5 illustrate the structures of Gal-3 WT and Gal-3 homodimer, respectively. Since both structures have identical CRDs, they yield equivalent potential of interaction forces when binding to ASF, supported by recent findings (Caballero et al., 2020). Consequently, the differences between the rupture forces in the lower range of loading rates could be a result of the different structural forms of the galectins.

As earlier mentioned, Gal-3 WT occurs as a monomer in solution, but has the ability to form a pentamer structure. The structure in which Gal-3 WT occurs determines the numbers of ASF molecules that can potentially bind to the galectin. If Gal-3 WT remains in the monomer form, only one ASF molecule can bind to the galectin at a given time. However, if the Gal-3 WT forms a pentamer structure, there are five active binding sites present,

allowing five ASF molecules to bind the galectin. Whereas, the engineered homodimer form of Gal-3 can only exist as a homodimer which is composed of two active binding sites. Consequently, enabling the binding of the ASF molecule through either one or two binding sites, thereby providing the potential of both single and multiple bonds for a single galectin molecule. As mentioned, based on the immobiliziation procedure, it is not possible to determine or observe the orientation of Gal-3 homodimer on the bead surface, as well as the structural form of Gal-3 WT.

Based upon the data obtained from the lower range of loading rates (up to around 100 pN/s), the rupture forces of the homodimer are higher than for the Gal-3 WT. Therefore, the differences in the interaction forces can be explained by the structure of Gal-3 WT, as well as the orientation of the homodimer. Due to the higher rupture forces Gal-3 homodimer attains, this can indicate that Gal-3 WT remains in its monomer structure in solution, which corresponds with earlier findings (Dam et al., 2005). This assumption also corresponds to the observations of higher loading rates in the current study and low frequency of rupture events during the measurements, as previously discussed. While the Gal-3 homodimer binds to the ASF through both CRDs, i.e. is orientated with both CRDs displayed toward the ligand, as illustrated in Figure 5.2a, hence providing higher interaction forces and the potential of multiple bindings with ASF.
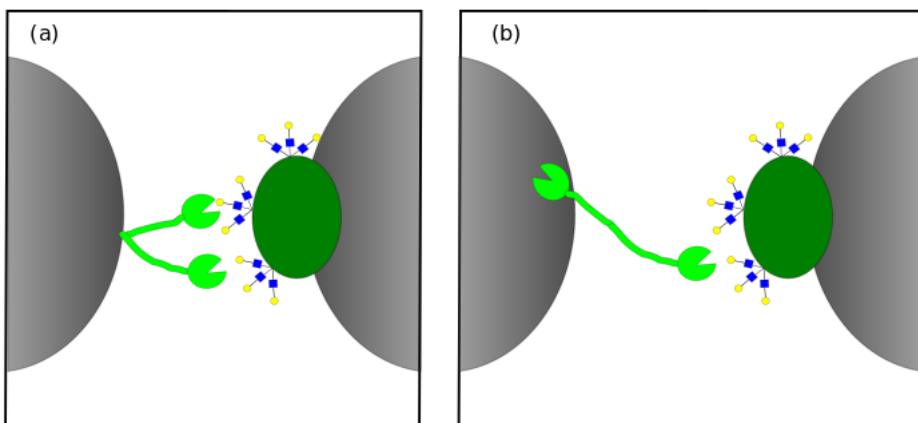

Figure 5.2: Suggestions of different orientations of the homodimer on the bead surface during the investigation of the interactions between Gal-3 homodimer and ASF. (a) The CRDs are pointing in the same direction, enabling both CRDs to interact with the ASF molecule. (b) The CRDs are pointing in the opposite direction, allowing only one CRD to interact with the ASF molecule.

Chapter 6

Conclusion

This master thesis presents the results obtained by using the sensitive force probe optical tweezers to study the interaction abilities of the two structural forms of Gal-3 with their ligand ASF. The results provide evidence that interactions between the two systems occur. By utilizing the Bell-Evans model, the properties of the energy landscape for both systems were identified. The rupture forces were found to range from 6.2 pN to 17.6 pN at loading rates between 39 pN/s and 406 pN/s for the Gal-3 WT - ASF system. For the Gal-3 homodimer - ASF system, the forces were found to vary between 5.7 pN and 27.8 pN at loading rates between 38 pN/s and 309 pN/s. The obtained parameters characterizing the energy landscape indicate that two energy barriers exist along the unbinding pathway for both systems, with a crossover between the energy barriers around 100 pN/s. However, there were observed high scattering among some of the determined parameters, leading to challenges in obtaining accurate values. Hence, more data is favourable in order to gain more reliable results. Additionally, implementing other DFS models can contribute to achieve more accurate results.

The comparison of the results obtained in this study display that the homodimer exhibited higher rupture forces, longer lifetime, as well as the shortest separation distance, in the low loading rate regime, compared to the WT. These findings can indicate that the WT is found as a monomer in solution, which in accordance with earlier findings. Additionally, the results can imply that the homodimer is orientated with both the CRDs displayed towards the ASF molecule, giving the potential of multiple bindings to the ligand.

Despite human lectins have been completely characterized structurally, the factors regard-

ing the specificity of glycan-lectin recognition are not yet fully understood. The results in the present study reveal the interaction abilities of different structural forms of Gal-3 with the same ligand. However, in future studies, it will be interesting to investigate other galectins, both natural and engineered forms, to uncover the interaction abilities of different galectins by aiming to relate protein design to activity. Thereby, eventually cracking the sugar code.

Bibliography

Ahmad, N., Gabius, H.-J., André, S., Kaltner, H., Sabesan, S., Roy, R., Liu, B., Macaluso, F., Brewer, C. F., 2004. Galectin-3 precipitates as a pentamer with synthetic multivalent carbohydrates and forms heterogeneous cross-linked complexes. Journal of Biological Chemistry 279 (12), 10841–10847.

Arangoa, M., Düzgüneş, N., De Ilarduya, C. T., 2003. Increased receptor-mediated gene delivery to the liver by protamine-enhanced-asialofetuin-lipoplexes. Gene therapy 10 (1), 5–14.

Ashkin, A., 1970. Acceleration and trapping of particles by radiation pressure. Physical review letters 24 (4), 156.

Bartolazzi, A., 2018. Galectins in cancer and translational medicine: From bench to bedside.

Belardi, B., Bertozzi, C. R., 2015. Chemical lectinology: tools for probing the ligands and dynamics of mammalian lectins in vivo. Chemistry & biology 22 (8), 983–993.

Binnig, G., Quate, C. F., Gerber, C., 1986. Atomic force microscope. Physical review letters 56 (9), 930.

Bizzarri, A. R., Cannistraro, S., 2010. The application of atomic force spectroscopy to the study of biological complexes undergoing a biorecognition process. Chemical Society Reviews 39 (2), 734–749.

Blázquez-Castro, A., 2019. Optical tweezers: Phototoxicity and thermal stress in cells and biomolecules. Micromachines 10 (8), 507.

Burgos-Bravo, F., Figueroa, N. L., Casanova-Morales, N., Quest, A. F., Wilson, C. A.,

Leyton, L., 2018. Single-molecule measurements of the effect of force on thy-1/$\alpha v \beta 3$-integrin interaction using nonpurified proteins. Molecular biology of the cell 29 (3), 326–338.

Caballero, G. G., Beckwith, D., Shilova, N. V., Gabba, A., Kutzner, T. J., Ludwig, A.-K., Manning, J. C., Kaltner, H., Sinowatz, F., Cudic, M., et al., 2020. Influence of protein (human galectin-3) design on aspects of lectin activity.

Chan, Y.-C., Lin, H.-Y., Tu, Z., Kuo, Y.-H., Hsu, S.-T. D., Lin, C.-H., 2018. Dissecting the structure–activity relationship of galectin–ligand interactions. International journal of molecular sciences 19 (2), 392.

Cummings, Richard D., F.-T. L., Vasta, G. R., 2017. Essentials of Glycobiology, 3rd Edition.

Cummings, R. D., Pierce, J. M., 2014. The challenge and promise of glycomics. Chemistry & biology 21 (1), 1–15.

Dam, T. K., Gabius, H.-J., André, S., Kaltner, H., Lensch, M., Brewer, C. F., 2005. Galectins bind to the multivalent glycoprotein asialofetuin with enhanced affinities and a gradient of decreasing binding constants. Biochemistry 44 (37), 12564–12571.

de Oliveira, J. T., Ribeiro, C., Gärtner, F., 2015. Role of galectin-3 in cancer metastasis. Glycobiology Insights (5).

De Vlaminck, I., Dekker, C., 2012. Recent advances in magnetic tweezers. Annual review of biophysics 41, 453–472.

Díaz-Alvarez, L., Ortega, E., 2017. The many roles of galectin-3, a multifaceted molecule, in innate immune responses against pathogens. Mediators of inflammation 2017.

Dudko, O. K., Hummer, G., Szabo, A., 2008. Theory, analysis, and interpretation of single-molecule force spectroscopy experiments. Proceedings of the National Academy of Sciences 105 (41), 15755–15760.

Dufrêne, Y. F., Ando, T., Garcia, R., Alsteens, D., Martinez-Martin, D., Engel, A., Gerber, C., Müller, D. J., 2017. Imaging modes of atomic force microscopy for application in molecular and cell biology. Nature nanotechnology 12 (4), 295.

Dufrêne, Y. F., Evans, E., Engel, A., Helenius, J., Gaub, H. E., Müller, D. J., 2011. Five challenges to bringing single-molecule force spectroscopy into living cells. nature methods 8 (2), 123–127.

Dulin, D., Cui, T. J., Cnossen, J., Docter, M. W., Lipfert, J., Dekker, N. H., 2015. High spatiotemporal-resolution magnetic tweezers: Calibration and applications for dna dynamics. Biophysical journal 109 (10), 2113–2125.

Dumic, J., Dabelic, S., Flögel, M., 2006. Galectin-3: an open-ended story. Biochimica et Biophysica Acta (BBA)-General Subjects 1760 (4), 616–635.

Evans, E., 1999. Introductory lecture energy landscapes of biomolecular adhesion and receptor anchoring at interfaces explored with dynamic force spectroscopy. Faraday discussions 111, 1–16.

Evans, E., Ritchie, K., 1997. Dynamic strength of molecular adhesion bonds. Biophysical journal 72 (4), 1541–1555.

Farhad, M., Rolig, A. S., Redmond, W. L., 2018. The role of galectin-3 in modulating tumor growth and immunosuppression within the tumor microenvironment. Oncoimmunology 7 (6), e1434467.

Farinha, D., de Lima, M. C. P., Faneca, H., 2014. Specific and efficient gene delivery mediated by an asialofetuin-associated nanosystem. International journal of pharmaceutics 473 (1-2), 366–374.

Friddle, R. W., Noy, A., De Yoreo, J. J., 2012. Interpreting the widespread nonlinear force spectra of intermolecular bonds. Proceedings of the National Academy of Sciences 109 (34), 13573–13578.

Gabius, H., 2017. How to crack the sugar code. Folia biologica 63 (4), 121–131.

Gabius, H.-J., 2018. The sugar code: why glycans are so important. Biosystems 164, 102–111.

Gerber, C., Lang, H. P., 2006. How the doors to the nanoworld were opened. Nature nanotechnology 1 (1), 3.

Hadjialirezaei, S., Picco, G., Beatson, R., Burchell, J., Stokke, B. T., Sletmoen, M., 2017. Interactions between the breast cancer-associated muc1 mucins and c-type lectin characterized by optical tweezers. PloS one 12 (4).

Håti, A. G., Aachmann, F. L., Stokke, B. T., Skjåk-Bræk, G., Sletmoen, M., 2015. Energy landscape of alginate-epimerase interactions assessed by optical tweezers and atomic force microscopy. PloS one 10 (10), e0141237.

Haug, Ø., 2017. Studies of muc1-gal3 lectin interaction by the sensitive force probe optical tweezers (ot). Master's thesis, NTNU.

Huang, M. L., Godula, K., 2016. Nanoscale materials for probing the biological functions of the glycocalyx. Glycobiology 26 (8), 797–803.

Hummer, G., Szabo, A., 2003. Kinetics from nonequilibrium single-molecule pulling experiments. Biophysical journal 85 (1), 5–15.

Instruments, JPK, n.d. Nanotracker 2. `https://www.jpk.com/products/force-sensing-optical-tweezers-and-optical-trapping/nanotracker-2`, last accessed 16 March 2020.

Johannes, L., Jacob, R., Leffler, H., 2018. Galectins at a glance. Journal of cell science 131 (9).

Johnson, K. C., Thomas, W. E., 2018. How do we know when single-molecule force spectroscopy really tests single bonds? Biophysical journal 114 (9), 2032–2039.

Kjær, S. O., 2018. Characterization of substrate binding and hybrid forming abilities of galectin-3. Master's thesis, NTNU.

Kutzner, T. J., Gabba, A., FitzGerald, F. G., Shilova, N. V., García Caballero, G., Ludwig, A.-K., Manning, J. C., Knospe, C., Kaltner, H., Sinowatz, F., et al., 2019. How altering the modular architecture affects aspects of lectin activity: case study on human galectin-1. Glycobiology 29 (8), 593–607.

Lakshminarayanan, A., Richard, M., Davis, B. G., 2018. Studying glycobiology at the single-molecule level. Nature Reviews Chemistry 2 (8), 148–159.

Li, M., Dang, D., Liu, L., Xi, N., Wang, Y., 2017. Imaging and force recognition of single molecular behaviors using atomic force microscopy. Sensors 17 (1), 200.

Linch, S., Kasiewicz, M. J., McNamara, M., Hilgart, I., Farhad, M., Redmond, W., 2015. Galectin-3 inhibition using novel inhibitor gr-md-02 improves survival and immune function while reducing tumor vasculature. Journal for immunotherapy of cancer 3 (S2), P306.

Ludwig, A.-K., Michalak, M., Xiao, Q., Gilles, U., Medrano, F. J., Ma, H., FitzGerald, F. G., Hasley, W. D., Melendez-Davila, A., Liu, M., et al., 2019. Design–functionality relationships for adhesion/growth-regulatory galectins. Proceedings of the National Academy of Sciences 116 (8), 2837–2842.

Mitsui, K., Hara, M., Ikai, A., 1996. Mechanical unfolding of a2-macroglobulin molecules with atomic force microscope. FEBS letters 385 (1-2), 29–33.

Motoyama, K., Nakashima, Y., Aramaki, Y., Hirayama, F., Uekama, K., Arima, H., 2011. In vitro gene delivery mediated by asialofetuin-appended cationic liposomes associated with γ-cyclodextrin into hepatocytes. Journal of drug delivery 2011.

Neuman, K. C., Block, S. M., 2004. Optical trapping. Review of scientific instruments 75 (9), 2787–2809.

Neuman, K. C., Chadd, E. H., Liou, G. F., Bergman, K., Block, S. M., 1999. Characterization of photodamage to escherichia coli in optical traps. Biophysical journal 77 (5), 2856–2863.

Neuman, K. C., Nagy, A., 2008. Single-molecule force spectroscopy: optical tweezers, magnetic tweezers and atomic force microscopy. Nature methods 5 (6), 491.

Ostrofet, E., Papini, F. S., Dulin, D., 2018. Correction-free force calibration for magnetic tweezers experiments. Scientific reports 8 (1), 1–10.

Ouerghi, O., Touhami, A., Othmane, A., Ouada, H. B., Martelet, C., Fretigny, C., Jaffrezic-Renault, N., 2002. Investigating antibody–antigen binding with atomic force microscopy. Sensors and Actuators B: Chemical 84 (2-3), 167–175.

Pfreundschuh, M., Alsteens, D., Wieneke, R., Zhang, C., Coughlin, S. R., Tampé, R., Kobilka, B. K., Müller, D. J., 2015. Identifying and quantifying two ligand-binding sites while imaging native human membrane receptors by afm. Nature communications 6 (1), 1–7.

Polimeno, P., Magazzu, A., Iatì, M. A., Patti, F., Saija, R., Boschi, C. D. E., Donato, M. G., Gucciardi, P. G., Jones, P. H., Volpe, G., et al., 2018. Optical tweezers and their applications. Journal of Quantitative Spectroscopy and Radiative Transfer 218, 131–150.

Radosavljevic, G., Volarevic, V., Jovanovic, I., Milovanovic, M., Pejnovic, N., Arsenijevic, N., Hsu, D. K., Lukic, M. L., 2012. The roles of galectin-3 in autoimmunity and tumor progression. Immunologic research 52 (1-2), 100–110.

Safenkova, I., Zherdev, A., Dzantiev, B., 2012. Application of atomic force microscopy for characteristics of single intermolecular interactions. Biochemistry (Moscow) 77 (13), 1536–1552.

Sciacchitano, S., Lavra, L., Morgante, A., Ulivieri, A., Magi, F., De Francesco, G. P., Bellotti, C., Salehi, L. B., Ricci, A., 2018. Galectin-3: one molecule for an alphabet of diseases, from a to z. International journal of molecular sciences 19 (2), 379.

Seyrek, K., Richter, M., Lavrik, I. N., 2019. Decoding the sweet regulation of apoptosis: The role of glycosylation and galectins in apoptotic signaling pathways. Cell Death & Differentiation 26 (6), 981–993.

Stangner, T., Wagner, C., Singer, D., Angioletti-Uberti, S., Gutsche, C., Dzubiella, J., Hoffmann, R., Kremer, F., 2013. Determining the specificity of monoclonal antibody hpt-101 to tau-peptides with optical tweezers. ACS nano 7 (12), 11388–11396.

Strick, T. R., Allemand, J.-F., Bensimon, D., Bensimon, A., Croquette, V., 1996. The elasticity of a single supercoiled dna molecule. Science 271 (5257), 1835–1837.

Wik, V. R., 2019. Interaksjoner mellom galektiner og deres substrater. Master's thesis, NTNU.

Yang, R.-Y., Hill, P. N., Hsu, D. K., Liu, F.-T., 1998. Role of the carboxyl-terminal lectin domain in self-association of galectin-3. Biochemistry 37 (12), 4086–4092.

Yu, Z., Dulin, D., Cnossen, J., Köber, M., van Oene, M. M., Ordu, O., Berghuis, B. A., Hensgens, T., Lipfert, J., Dekker, N. H., 2014. A force calibration standard for magnetic tweezers. Review of scientific instruments 85 (12), 123114.

Appendix

Statistical analysis

Standard deviation

Standard deviation for all measurements were determined by the built in Excel function STDAV.S with following formula;

$$\sigma = \sqrt{\frac{\sum(x_i - \overline{x})^2}{N-1}} \qquad (6.1)$$